

# Synthesis and Characterization of New Polymeric Ionic Liquids as Corrosion Inhibitors for Carbon Steel in a Corrosive Medium: Experimental, Spectral, and Theoretical Studies

Hend Asfour, Ghada Y. Elewady, Elsayed G. Zaki, and Abd El-Aziz S. Fouda\*



Cite This: *ACS Omega* 2023, 8, 41077–41099



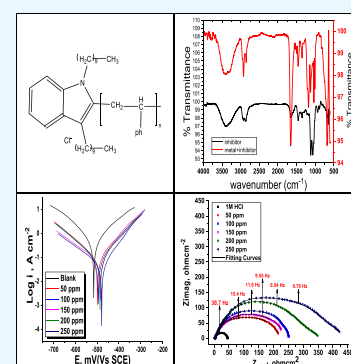
Read Online

ACCESS |

Metrics & More

Article Recommendations

**ABSTRACT:** A novel series of polymeric ionic liquids (ILs) based on benzimidazolium chloride derivatives, namely, 1,3-diheptyl-2-(2-phenyl-propyl)-3*H*-benzimidazol-1-ium chloride (IL1), 1,3-dioctyl-2-(2-phenyl-propyl)-3*H*-benzimidazol-1-ium chloride (IL2), and 1,3-Bis-decyl-2-(2-phenyl-propyl)-3*H*-benzimidazol-1-ium chloride (IL3), were synthesized and chemically elucidated by Fourier transform infrared spectroscopy,  $^1\text{H}$  NMR,  $^{13}\text{C}$  NMR, and elemental analysis. Their influence as corrosion suppressors were investigated for C-steel corrosion in 1 M HCl, by weight loss (WL), potentiodynamic polarization (PDP), and electrochemical impedance spectroscopy (EIS) methods, revealing that their exclusive addition decreased corrosion with mounting concentrations. These assays demonstrated that novel ILs are efficient inhibitors at relatively low dosages. The efficacy of the synthesized ILs reached 79.7, 92.2 and 96.9%, respectively, at 250 ppm and 303 K. Parameters for activation and adsorption were calculated and are discussed. The Tafel polarization results demonstrated that the investigated ILs support the suppression of both cathodic and anodic reactions, acting as mixed type inhibitors. Langmuir's adsorption isotherm was confirmed as the best fitted isotherm, describing the physical–chemical adsorption capability of used ILs on the C-steel surface with the change in the free energy of adsorption,  $\Delta G_{\text{ads}}^{\circ} = 32.6\text{--}37.2$  kJ mol $^{-1}$ . The efficacy of the synthesized ILs was improved by increasing the doses, and the temperature reached 86.6, 96.1, and 98.4%, respectively, at 318 K. Surface morphology was proved by Fourier Transform Infrared spectroscopy, X-ray photoelectron spectroscopy, and atomic force microscopy (AFM), and then, changes in test solutions were checked by Ultraviolet–visible spectroscopy. Theoretical modeling (density functional theory and Monte Carlo) revealed the correlation between the IL's molecular chemical structure and its anticorrosive property.



## 1. INTRODUCTION

Studying the corrosion inhibition is a big deal for two reasons. Economically, inhibition reduces material loss such as sudden failure of piping, structures, etc. It also helps the conservation of limited metal resources and reduces water and energy loss accompanying the metal structure fabrication.<sup>1</sup> Carbon steel is largely used in the oil and natural gas processing industry for its strength, ductility, low cost, availability, and mechanical characteristics.<sup>2,3</sup> Hydrochloric acid solutions are presently used in the descaling, pickling, and electrochemical etching process under drastic conditions.<sup>4–8</sup> The chloride ions of the acid cause passivity collapse and inception of pitting corrosion.<sup>9</sup> For the preceding reasons, it is essential to find an inhibitor to diminish the corrosion of C-steel. Ionic liquids (ILs) have proved to be promising corrosion inhibitors for steel according to the review of the literature<sup>10–14</sup> as they are a liquid-shaped salt with a low melting point, consisting of an organic cation and variable anions and they exhibit low toxicity, incombustibility, and good chemical and thermal stability.<sup>15–18</sup> The use of polymeric ILs based on benzimidazolium chloride derivatives as inhibitors is due to their

physicochemical adsorption properties depending on atomic nitrogen as the reaction center stabilizing the adsorption and intramolecular proton transfer, enhancing adsorption at the metal/corrosive medium interface and thus preventing corrosion.<sup>19</sup> One of the most significant groups of ILs is the imidazole-based one, which has a number of benefits including safety, affordability, nontoxicity, biodegradability, water solubility, strong metal adsorption, and good protective effectiveness.<sup>20</sup> ILs based on imidazole often exhibit different levels of inhibition depending on the size and length of their alkyl chains.<sup>21</sup> The corrosion rate reduces as the number of alkyl chains is increased in the presence of the inhibitor, indicating inhibitor adsorption on the metal surface and prevention of corrosion of the metal.<sup>22</sup> Additionally, the

Received: May 18, 2023

Revised: September 7, 2023

Accepted: October 16, 2023

Published: October 27, 2023



Table 1. Formulas and Chemical Structures of ILs

Chemical structure	Code name	Mol. formula and Mol. Wt.	IUPAC Name
	IL1	C <sub>30</sub> H <sub>40</sub> N <sub>2</sub> Cl 483.5	1,3-Diheptyl-2-(2-phenyl-propyl)-3H-benzimidazol-1-ium chloride
	IL2	C <sub>32</sub> H <sub>49</sub> N <sub>2</sub> Cl 496.5	1,3-Dioctyl-2-(2-phenyl-propyl)-3H-benzimidazol-1-ium chloride
	IL3	C <sub>36</sub> H <sub>57</sub> N <sub>2</sub> Cl 552.5	1,3-Bis-decyl-2-(2-phenyl-propyl)-3H-benzoimidazol-1-ium chloride

presence of a free nitrogen atom in an imidazole compound causes the development of a hydrophobic coating on the metal surface, which lessens the attack of chloride ions or any other corrosive environment on the metal surface. The recommended proposal is for them to be introduced as efficient corrosion inhibitors to fire water, which mostly contains chloride ions, in order to preserve the whole fire water pipe system from corrosion.<sup>23</sup> The effect of Si and P content in steel (steel/class A, steel/class B, and steel/class C) suitable for galvanizing on its corrosion inhibition in 5 M HCl solution without and with cetyltrimethylammonium combined with KI (mixture) was studied.<sup>24</sup> The inhibition efficiency was about 97, 92, and 76% for the three classes A, B, and C, respectively. Rbaa<sup>25</sup> synthesized and characterized novel quinoline (Q-CH<sub>3</sub>, Q-Br, and Q-H) derivatives, and then, they were evaluated as inhibitors against corrosion of mild steel in 1.0 M HCl. The inhibitory efficiency reached 96, 95.3, and 95.2% for  $1 \times 10^{-3}$  M Q-CH<sub>3</sub>, Q-Br, and Q-H compounds, respectively. In an acidic condition, Sasikumar et al.<sup>26</sup> looked at the inhibitory behavior of 1-decyl-3-methylimidazolium tetra fluoroborate for mild steel. It was discovered that this chemical has a good mild steel inhibition efficacy in 1 M HCl solution. The three ILs (IL2, IL3, and IL6) containing quaternary N with long alkyl-saturated chains (cation) and bromide (anion) showed corrosion inhibition properties for the protection of C-steel in aqueous 1 M HCl, according to the research by Tawfik<sup>27</sup> The effectiveness of these compounds is dependent on the formation of a barrier between the corroding medium and the metal. Inhibitor adsorption can occur either physically or chemically. The former involves the formation of an electrostatic attraction between the charged metal and the charged inhibitor molecules, whereas the latter involves charge transfer and the formation of a coordinate-type bond between the inhibitor and metal surface.<sup>28–30</sup>

The high inhibition properties of ILs, including their pH stability, low toxicity, economical preparation, low volatility (accounting for their low tendency of contaminating the environment), and high chemical and thermal stability characteristics, are better than those of conventional inhibitors. IL compounds have low melting point, high conductivity, and negligible vapor pressure, so they are considered environ-

mental corrosion inhibitors. As such, we utilized ILs as corrosion inhibitors for C-steel in 1 M HCl.

The objective of our work was to design a series of three polymeric ILs (i.e., 1,3-diheptyl-2-(2-phenyl-propyl)-3H-benzimidazol-1-ium chloride (IL1), 1,3-dioctyl-2-(2-phenyl-propyl)-3H-benzimidazol-1-ium chloride (IL2), and 1,3-dioctyl-2-(2-phenyl-propyl)-3H-benzimidazol-1-ium chloride) (IL3). The goal of this study is to determine how the presence of more methyl group substituents in imidazolium ILs with long alkyl chains affects the ability of the C-steel to resist corrosion. The electrochemical impedance spectroscopy (EIS), potentiodynamic polarization (PDP), and weight loss (WL) methodologies were used to investigate the effectiveness of the inhibitor. The Langmuir adsorption isotherm was employed to demonstrate the presence of inhibitors on C-steel. Ultraviolet (UV) spectra were used to investigate how inhibitors and C-steel interact. The alterations on the metal surface with and without inhibitors were examined using X-ray photoelectron spectroscopy (XPS), atomic force microscopy (AFM), Fourier transform infrared (FTIR) spectroscopy, and scanning electron microscopy (SEM). The structure of the formed polymeric ILs was demonstrated using FTIR spectroscopy, <sup>1</sup>H NMR, and <sup>13</sup>C NMR, and their structures, molecular weights, and formulas are displayed in (Table 1).

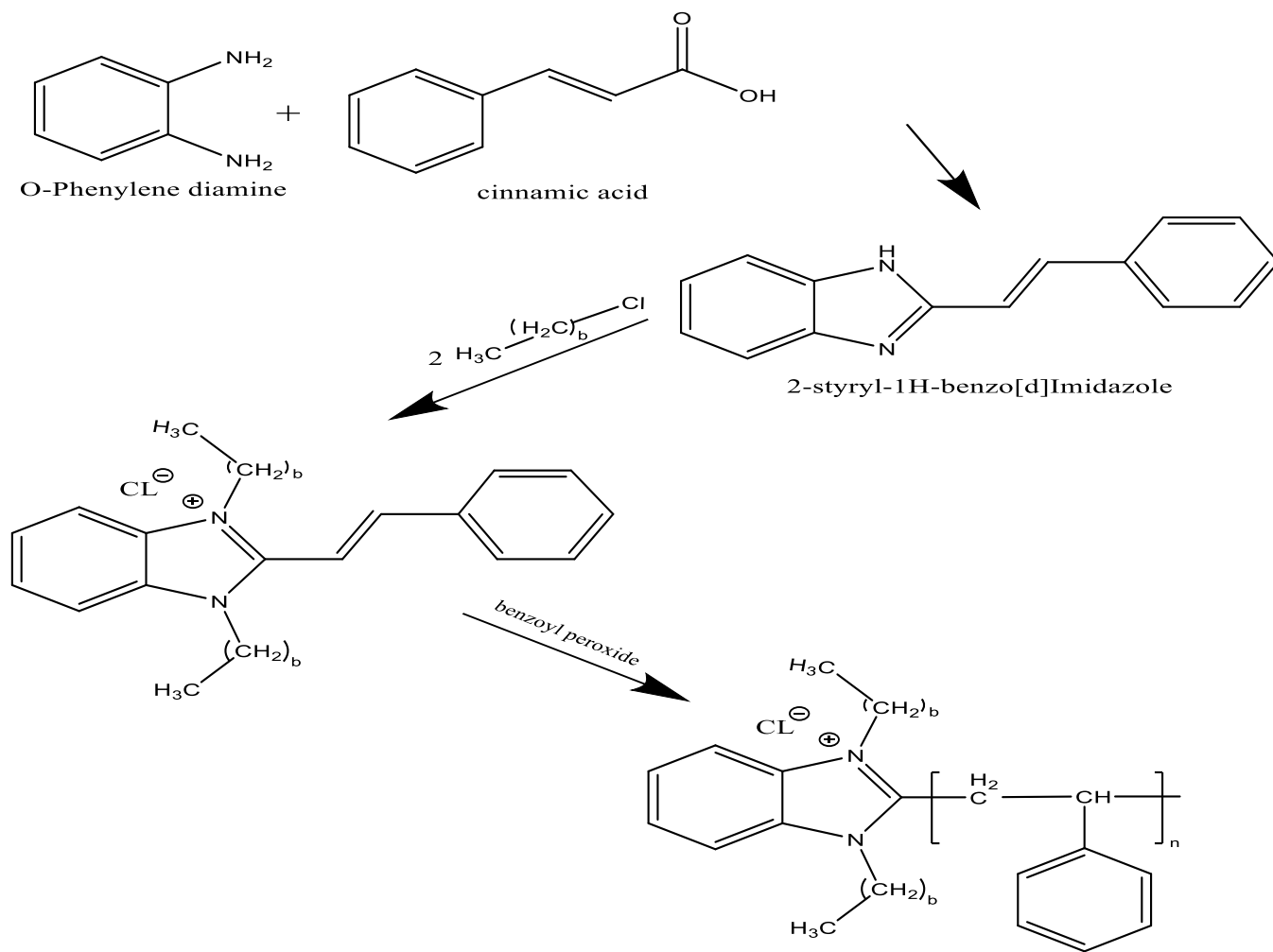
## 2. EXPERIMENTAL SECTION

### 2.1. Materials and Reagents. 2.1.1. C-Steel Specimens.

C-steel with the composition C 0.2%, Mn 0.35%, P 0.024%, Si 0.003%, and Fe remaining was attained from the Central Metallurgical Research Institute, and it was mechanically cut into coupons of  $2 \times 2 \times 0.1$  cm dimensions for WL measurements and of  $1 \times 1 \times 0.1$  cm dimensions that were then welded with the Cu wire for electrochemical measurements. Samples were prepared in the laboratory by being scrubbed with numerous abrasive sandpapers ranging from 180 to 2000), and they were soaked in acetone as a degreasing solution, washed with double-distilled water, dried between two filter papers, resulting in mirror-like finish, and kept in desiccator.

**2.1.2. IL Manufacturing.** The synthesis operation was carried out in the Egyptian Petroleum Research Institute. The synthesis route was launched in three steps:

Scheme 1. Synthesis Route of the Investigated ILs



**2.1.2.1. Step One (Forming Benzimidazole of Styryl).** *O*-Phenylenediamine and cinnamic acid were dissolved in ethanol and mixed in an equimolar proportion. The mixture was then refluxed for 6 h at 75 °C. To be basified, the reaction mixture was cooled followed by the addition of sodium carbonate solution. Upon adding 20 mL of cold water, the product was precipitated, yielding benzimidazole of styryl.

**2.1.2.2. Step Two (Forming the Monomers).** The first step product (0.01 mol) was dissolved in ethanol, and after, potassium hydroxide (0.02 mol) was added. For 90 min, the mixture was stirred at 70 °C, accompanied by dropwise addition of 1-chloro-2,4-dimethylpentane IL1, 1-chlorooctane IL2, and chlorodecane IL3 (0.02 mol) to the stirred reaction mixture. The mixture was then cooked for 24 h at 7080 °C; thereafter, it was cooled to room temperature. The material was then extracted with ethanol, washed with ethyl acetate, filtered, and eventually dried to yield oily products.

**2.1.2.3. Step Three (Polymerization).** In water, ILs (1–3) (0.001 mol) were dissolved, and then, sodium benzoate was added (0.001 mol.). For 6 h, the mixture was refluxed and then treated with benzoyl peroxide (0.5 wt % monomer); then, the temperature was increased to 70 °C and sustained for around 10 h. The reaction liquid was then cooled, and 250 mL of acetone was added. The precipitates generated were filtered out, washed with 100% methanol and diethyl ether, and lastly

dried under vacuum at 20 °C. ILs (1–3) were assigned to the polymer that was produced (Scheme 1).

**2.1.3. Solutions.** The aggressive solution was prepared from HCl of analytical grade (37%), which was purchased from Algamhoria.co, Egypt. The desired concentration of HCl was determined by dilution with double-distilled water and confirmed with titration against sodium carbonate standard solution. Double-distilled water was used as well for preparing 1000 ppm stock solutions of ILs.

**2.2. WL Method.** At room temperature (25 °C), seven prepared C-steel coupons were weighted precisely using a sensitive balance (Sartorius GM1502) and then immersed in (1 M) HCl blank solution and in six different inhibitor concentrations mixed with (1 M) HCl in each. After half an hour, the coupons were cleaned, dried, and weighed precisely; then, we repeated these steps 6 times. The average WLs ( $\text{mg cm}^{-2}$ ) were recoded, and then, eq 1 was applied to calculate the inhibition percentage [9]

$$\text{IE \%} = \theta \times 100 = \left[ 1 - \frac{w}{w^{\circ}} \right] \times 100 \quad (1)$$

where  $\theta$  is the surface coverage and  $W$  and  $W^{\circ}$  are the average WLs in the presence and absence of inhibitors, respectively. The preceding steps were carried out at 30, 35, 40, and 45 °C.

**2.3. Electrochemical Measurements.** The electrochemical experiments were performed in a glass reaction reactor

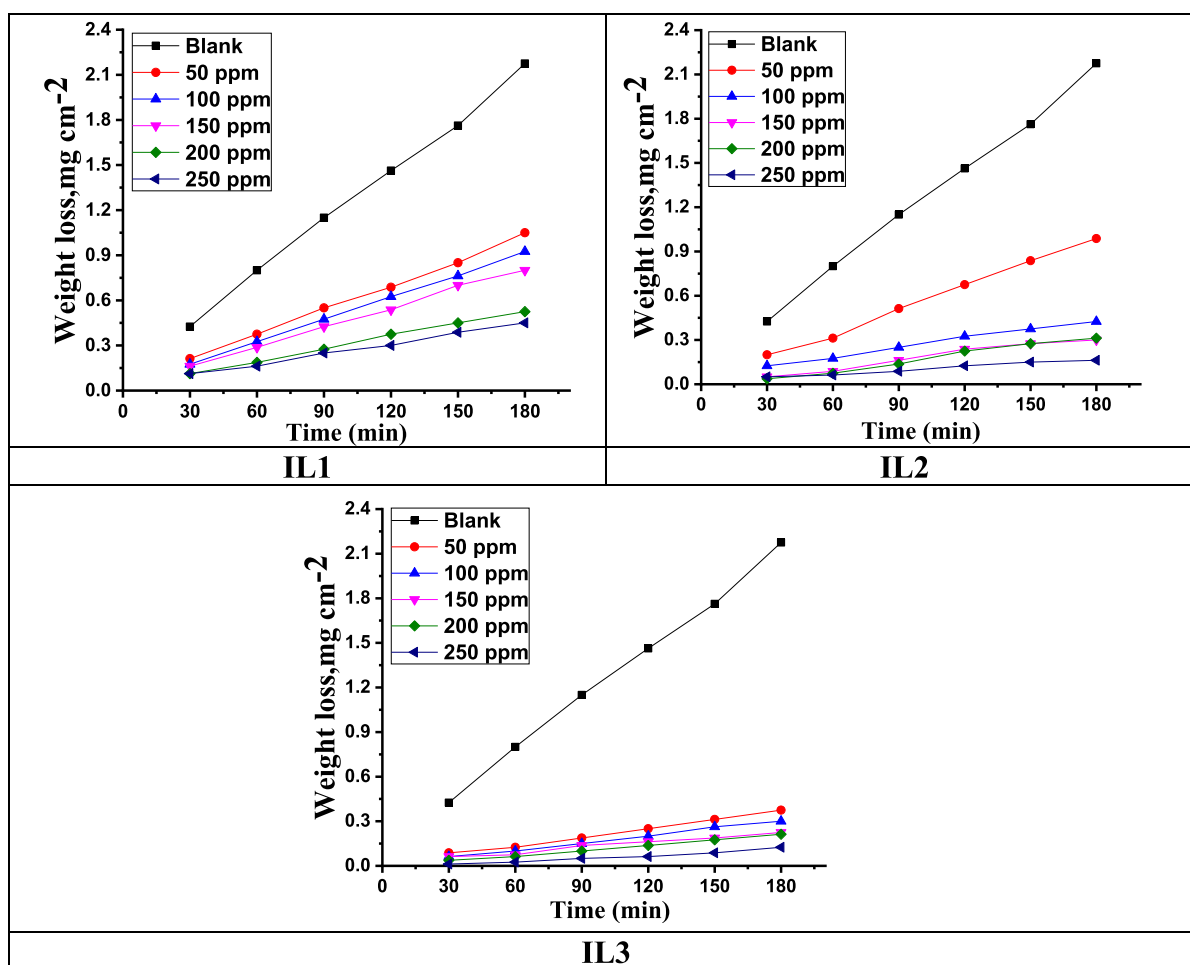


**Figure 1.** WL–time graphs of C-steel in 1 M HCl with and without different concentrations of various ILs at 298 K.

involving three electrodes. A working electrode fabricated from C-steel ( $1 \text{ cm}^2$ ) welded with the Cu wire and prepared in the same manner as in the WL method, a counter electrode made from platinum foil ( $1 \text{ cm}^2$ ), and a standard calomel electrode (SCE) obtained via the Luggin capillary were used. All three were embedded in epoxy resins to expose the desired unified geometrical surface area and then dipped in freshly prepared test solution at room temperature and stabilized for 30 min before each experiment until they reached the steady state under the unstirred condition. The potentials are displayed versus normalized hydrogen electrode.

PDP involves sweeping the potential in the positive direction till 500 mV and then reversing the direction toward negative till  $-500 \text{ mV}$  at a scan rate of  $0.1 \text{ mVs}^{-1}$ . The inhibition percentage is calculated from eq 2<sup>31</sup>

$$\text{IE}_{\text{pp}} \% = \theta \times 100 = [(i_{\text{corr}(\text{blank})} - i_{\text{corr}}) / i_{\text{corr}(\text{blank})}] \times 100 \quad (2)$$

where  $i_{\text{corr}}$  and  $i_{\text{corr}(\text{blank})}$  are current densities in the presence and absence of inhibitors, respectively.

For EIS, we recorded results in the frequency range of  $1 \times 10^5$  to  $0.1 \text{ Hz}$  and at an amplitude of  $10 \text{ mV}$ . The charge transfer resistance was used to calculate IE % as shown in eq 3.<sup>32</sup>

$$\text{IE \%} = \theta \times 100 = \left[ 1 - \frac{R_{\text{ct}}^{\circ}}{R_{\text{ct}}} \right] \times 100 \quad (3)$$

where  $R_{\text{ct}}$  and  $R_{\text{ct}}^{\circ}$  are charge transfer resistances in the presence and absence of inhibitors, respectively.

Electrochemical measurements were carried out using Origastate instruments (origastate 080), and then, the graphing, fitting, and recording were performed using Origa master 5. All experiments were performed at 298 K.

**2.4. Metal Surface Analysis.** Analyzing the C-steel surface is crucial to identify the morphology, proving the adsorption of the ILs and allowing the assessment of their impact as inhibitors.<sup>33</sup> Our specimens were prepared by grinding the C-steel coupons to a grit of 4000 and then polishing with several sandpapers. The prepared metal sheets were immersed in 1 M HCl solution for 24 h at 298 K without the addition of the inhibitors to evaluate the influence of the corrosive medium on the metal morphology. Analogous actions were conducted but with 250 ppm inhibitor solutions. These investigations were fulfilled by FTIR spectroscopy (PerkinElmer-1430 Infrared spectrophotometer (Waltham MA)), AFM (model FlexAFM3), and XPS (AXIX Ultra DLD, Kratos, UK).

**2.5. Test Solution Analysis.** Degreased and cleaned C-steel coupons were dipped in the corrosive solution (1 M HCl) and left for 24 h at 298 K; then, the test solutions were examined by UV–visible (UV–vis) spectroscopy with a scan range (190–1100 nm). The same steps were carried out in the same way with the addition of 250 ppm solutions of inhibitors. The shift in the band wavelength and color change were

noticed. In this spectral analysis, we used a UV–vis spectrophotometer (16-1884-18-0030).

**2.6. Density Functional Theory and Monte Carlo Simulations.** Density functional theory (DFT) and Monte Carlo simulation of the cationic forms of ILs in aqueous solution were performed using DMol3 and adsorption factor modulation through material studio v.7.0 (by Accelrys Inc. USA).<sup>34</sup> The molecules were optimized by choosing B3LYB (Becke-3-parameters-lee-yang-parr) with DNP functions while setting the fine quality. Fine convergence and global orbital cutoffs were utilized as well as setting water as the solvent, which impacts the treatment via COSMO controls.<sup>35</sup> The simulation of IL adsorption on an Fe (1 1 0) crystal via the adsorption factor module was used to assess the impact of their inhibitory trail.<sup>36</sup> The Fe (1 1 0) crystal and the inhibitors interaction was designed in a simulation box (32.27 Å × 32.27 Å × 50.18 Å) via periodic boundary conditions.<sup>37</sup> The optimization of the inhibitor energy was done by the Forcite simulation engine.<sup>38</sup> Fe (1 1 0), water molecules, and manufactured ILs are engaged in building the corrosion inhibition system. Compass simulation along with the force field were implemented for ILs on an Fe (1 1 0) optimized surface.<sup>39</sup> In terms of  $I_p$  and  $E_A$ , the following equations were used to determine the global hardness ( $\eta$ ), softness ( $\sigma$ ), and chemical potential ( $\mu$ )<sup>40</sup>

$$\mu = -\chi = -\frac{I_p + E_A}{2} \quad (4)$$

$$\chi = -\frac{I_p + E_A}{2} \quad (5)$$

$$\eta = -\frac{I_p + E_A}{2} \quad (6)$$

$$\sigma = -\frac{1}{\eta} \quad (7)$$

### 3. RESULTS AND DISCUSSION

**3.1. Compounds Characterization.** **3.1.1. Compound (1).** 1,3-Diheptyl-2-(2-phenyl-propyl)-3H-benzimidazol-1-ium chloride, C<sub>30</sub>H<sub>40</sub>N<sub>2</sub>Cl (M. wt.: 469.15).

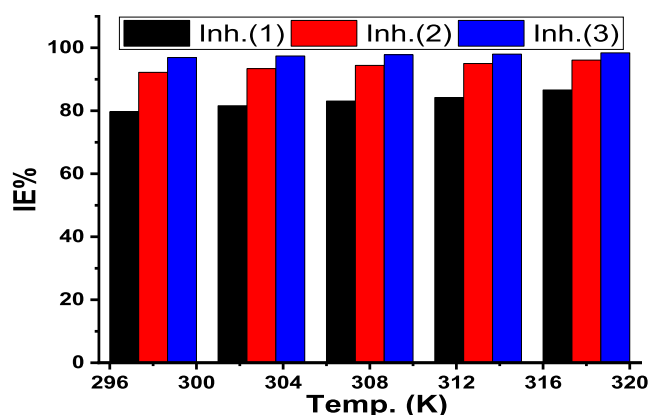


Figure 2. Graph between IE % and temperature of all ILs at 250 ppm.

Elemental analysis: calculated (found): C: 76.80 (76.82), H: 9.67 (9.71), N: 5.97 (5.80), Cl: 7.56 (7.67).

**Table 2. Representing  $K_{\text{corr}}$ ,  $\theta$ , and IE % for C-Steel in 1 M HCl with and without Different Concentrations of Inhibitors at 298 K**

inhibitors	conc., (ppm)	$k_{\text{corr}}$ , mg cm <sup>-2</sup> min <sup>-1</sup>	$\theta$	IE %
blank	0.0			
IL1	50	0.0063	0.531	53.1
	100	0.0050	0.594	59.4
	150	0.0048	0.641	64.1
	200	0.0030	0.766	76.6
	250	0.0027	0.797	79.7
IL2	50	0.0052	0.609	60.9
	100	0.0030	0.781	78.1
	150	0.0015	0.891	89.1
	200	0.0011	0.906	90.6
	250	0.0010	0.922	92.2
IL3	50	0.0021	0.844	84.4
	100	0.0020	0.875	87.5
	150	0.0012	0.906	90.6
	200	0.0010	0.922	92.2
	250	0.0004	0.969	96.9

FTIR (S1): the 2955 cm<sup>-1</sup> peak is assigned to aromatic hydrogens and 2925 and 2852.58 cm<sup>-1</sup> are related to the symmetric and asymmetric C–H stretching, respectively, C=N stretching bands appear at 1649 cm<sup>-1</sup>, C=C stretching bands appear at 1626 cm<sup>-1</sup>, and the C–N vibrational band appears at 1561 cm<sup>-1</sup>. The band at 1321 cm<sup>-1</sup> is assigned to C–H bending and that at 727 cm<sup>-1</sup> is assigned to C–H in the (CH<sub>2</sub>)<sub>n</sub> skeleton. The broad band at 3397 at cm<sup>-1</sup> is for CH...H<sub>2</sub>O hydrogen bonding, and all of this is accompanied by the disappearance of the vinyl band, attributed to polymerization.

<sup>1</sup>H NMR (S4) (500 MHz, DMSO-*d*<sub>6</sub>): 1.537 (2H, [CH<sub>2</sub>–CH–Ph]), 1.162 (6H, CH<sub>3</sub>), 2.195–3.857 (24H, aliphatic protons, CH<sub>2</sub>), 2.187 (1H, [CH<sub>2</sub>–CH–Ph]), 7.049–8.854 (9H, aromatic protons, CH).

<sup>13</sup>C NMR (S7) (125 MHz, DMSO-*d*<sub>6</sub>): 35.906 ([CH<sub>2</sub>–CH–Ph]), 13.519 (CH<sub>3</sub>), 21.655–71.922 (aliphatic carbons, CH<sub>2</sub>), 38.185 ([CH<sub>2</sub>–CH–Ph]), 160.819 (C=N), 126.329–147.485 (aromatic carbons, CH).

**3.1.2. Compound (2).** 1,3-Dioctyl-2-(2-phenyl-propyl)-3H-benzimidazol-1-ium chloride, C<sub>32</sub>H<sub>49</sub>N<sub>2</sub>Cl (M. wt.: 497.21).

Elemental analysis: calculated (found): C: 77.30 (77.44), H: 9.93 (9.72), N: 5.63 (5.55), Cl: 7.13 (7.29).

FTIR (S2): 2925 and 2871 cm<sup>-1</sup> peaks are related to the symmetric and asymmetric C–H stretching, respectively, the C=N stretching band appears at 1652 cm<sup>-1</sup>, and the C–N vibrational band appears at 1560 cm<sup>-1</sup>. The bands at 1353 cm<sup>-1</sup> is assigned to C–H bending, that at 723 cm<sup>-1</sup> is assigned to C–H in the (CH<sub>2</sub>)<sub>n</sub> skeleton, and the broad band at 3399 at cm<sup>-1</sup> is for CH...H<sub>2</sub>O hydrogen bonding. All of this is accompanied by the disappearance of the vinyl band, attributed to polymerization.

<sup>1</sup>H NMR (S5) (500 MHz, DMSO-*d*<sub>6</sub>): 1.543 (2H, [CH<sub>2</sub>–CH–Ph]), 1.163 (6H, CH<sub>3</sub>), 2.323–2.788 (28H, aliphatic protons, CH<sub>2</sub>), 2.300 (1H, [CH<sub>2</sub>–CH–Ph]), 4.320–7.494 (9H, aromatic protons, CH).

<sup>13</sup>C NMR (S8) (125 MHz, DMSO-*d*<sub>6</sub>): 31.364 ([CH<sub>2</sub>–CH–Ph]), 14.023 (CH<sub>3</sub>), 22.169–72.426 (aliphatic carbons, CH<sub>2</sub>), 36.429 ([CH<sub>2</sub>–CH–Ph]), 166.446 (C=N), 99.477–146.377 (aromatic carbons, CH).

Table 3. Variation of (IE %) and ( $\theta$ ) for Various Concentrations of Investigated ILs at Different Temperatures

temp., K	inhibitors	[Inh] ppm	$k_{\text{corr}}$ (mg cm <sup>-2</sup> min <sup>-1</sup> )	$\theta$	IE %	temp., K	inhibitors	[Inh] ppm	$k_{\text{corr}}$ (mg cm <sup>-2</sup> min <sup>-1</sup> )	$\theta$	IE %
303	blank	0.0	0.0160			313	blank	0.0	0.0210		
	IL1	50	0.0067	0.579	57.9		IL1	50	0.0073	0.653	65.3
		100	0.0060	0.645	63.2			100	0.0075	0.663	66.3
		150	0.0050	0.648	68.4			150	0.0054	0.743	74.3
		200	0.0035	0.803	80.3			200	0.0045	0.812	81.2
		250	0.0029	0.816	81.6			250	0.0033	0.842	84.2
	IL2	50	0.0054	0.658	65.8		IL2	50	0.0058	0.723	72.3
		100	0.0035	0.789	78.9			100	0.0045	0.822	82.2
		150	0.0017	0.895	89.5			150	0.0021	0.901	90.1
		200	0.0012	0.921	92.1			200	0.0016	0.941	94.1
		250	0.0011	0.934	93.4			250	0.0013	0.950	95.0
	IL3	50	0.0023	0.855	85.5		IL3	50	0.0027	0.871	87.1
		100	0.0021	0.895	89.5			100	0.0023	0.901	90.1
		150	0.0015	0.908	90.8			150	0.0019	0.911	91.1
		200	0.0011	0.934	93.4			200	0.0013	0.950	95.0
250		0.00042	0.974	97.4	250	0.00046		0.980	98.0		
308	blank	0.0	0.0190			318	blank	0.0	0.0260		
	IL1	50	0.0071	0.618	61.8		IL1	50	0.0081	0.693	69.3
		100	0.0070	0.646	64.6			100	0.008	0.717	71.7
		150	0.0052	0.719	71.9			150	0.0055	0.787	78.7
		200	0.0040	0.809	80.9			200	0.0050	0.819	81.9
		250	0.0031	0.831	83.1			250	0.0035	0.866	86.6
	IL2	50	0.0056	0.697	69.7		IL2	50	0.0060	0.772	77.2
		100	0.0040	0.809	80.9			100	0.0050	0.827	82.7
		150	0.0019	0.899	89.9			150	0.0023	0.913	91.3
		200	0.0014	0.933	93.3			200	0.0018	0.953	95.3
		250	0.0012	0.944	94.4			250	0.0014	0.961	96.1
	IL3	50	0.0025	0.865	86.5		IL3	50	0.0029	0.89	89
		100	0.0022	0.899	89.9			100	0.0024	0.913	91.3
		150	0.0017	0.910	91.0			150	0.0021	0.921	92.1
		200	0.0012	0.944	94.4			200	0.0014	0.961	96.1
250		0.00044	0.978	97.8	250	0.00048		0.984	98.4		

**3.1.3. Compound (3).** 1,3-Bis-decyl-2-(2-phenyl-propyl)-3H-benzimidazole-ium chloride, C<sub>36</sub>H<sub>57</sub>N<sub>2</sub>Cl (M. wt.: 553.32).

Elemental analysis: calculated (found): C: 78.15 (78.30), H: 10.38 (10.35), N: 5.06 (5.13), Cl: 6.41 (6.22).

FTIR (S3): 2923 and 2876.9 cm<sup>-1</sup> peaks are related to the symmetric and asymmetric C–H stretching, the C=N stretching band appears at 1652 cm<sup>-1</sup>, and the C–N vibrational band appears at 1458 cm<sup>-1</sup>. The band at 1353 cm<sup>-1</sup> is assigned to C–H bending, that at 724 cm<sup>-1</sup> is assigned to C–H in the (CH<sub>2</sub>)<sub>n</sub> skeleton, and the broad band at 3393 cm<sup>-1</sup> is for CH...H<sub>2</sub>O hydrogen bonding. All of this is accompanied by the disappearance of the vinyl band, attributed to polymerization.

<sup>1</sup>H NMR (S6) (500 MHz, DMSO-*d*<sub>6</sub>): 1.525 (2H, [CH<sub>2</sub>–CH–Ph]), 1.160 (6H, CH<sub>3</sub>), 2.197–4.071 (36H, aliphatic protons, CH<sub>2</sub>), 2.187 (1H, [CH<sub>2</sub>–CH–Ph]), 6.911–8.150 (9H, aromatic protons, CH).

<sup>13</sup>C NMR (S9) (125 MHz, DMSO-*d*<sub>6</sub>): 36.371 ([CH<sub>2</sub>–CH–Ph]), 12.087 (CH<sub>3</sub>), 22.131–72.388 (aliphatic carbons, CH<sub>2</sub>), 40.425 ([CH<sub>2</sub>–CH–Ph]), 161.314 (C=N), 123.008–167.781 (aromatic carbons, CH).

**3.2. WL Method.** **3.2.1. Effect of the Concentration Change.** The WL method is a frequently used strategy providing direct relativity between causes and effects<sup>41</sup> besides being independent of expensive equipment. We used the

immersion test of prepared C-steel sheets in 1 M HCl in the presence and absence of altered doses of used ILs at 298 K, obtaining a linear relationship between the WL and time (*t*), as shown in Figure 1. Figure 2 shows double plots of two *y*-axes ( $k_{\text{corr}}$ , IE %) versus the *x*-axis [different IL concentrations (ppm)] at 298 K calculated from eqs 8 and 9

$$k_{\text{corr}} = \text{WL}/S_A t \quad (8)$$

$$\text{IE \%} = [(k_{\text{corr}}^{\circ} - k_{\text{corr}})/k_{\text{corr}}^{\circ}] \quad (9)$$

where  $k_{\text{corr}}$  and  $k_{\text{corr}}^{\circ}$  are the corrosion rates (mg cm<sup>-2</sup> min<sup>-1</sup>) with and without the addition of inhibitors, respectively, IE % is the inhibition efficiency,  $S_A$  is the surface area of metal sheets, and *t* is the time in minutes. Values tabulated in Table 2 show that IE % of the utilized ILs (1, 2, and 3) is promoted with mounting concentrations until reaching 79.7, 92.2, and 96.9%, respectively, at the optimum concentration (250 ppm), after which the inhibition exhibits a steady state. The increased inhibitory action is attributed to IL adsorption on the metal surface, forming a protective film, which diminishes the  $k_{\text{corr}}$ <sup>42</sup> while the steady state after the optimum concentration is attributed to the surface being saturated with the inhibitors. All used ILs are showing the same behavior, taking into consideration that IE % is arranged as follows: IL3 > IL2 > IL1, which suggests that extending the carbon chain

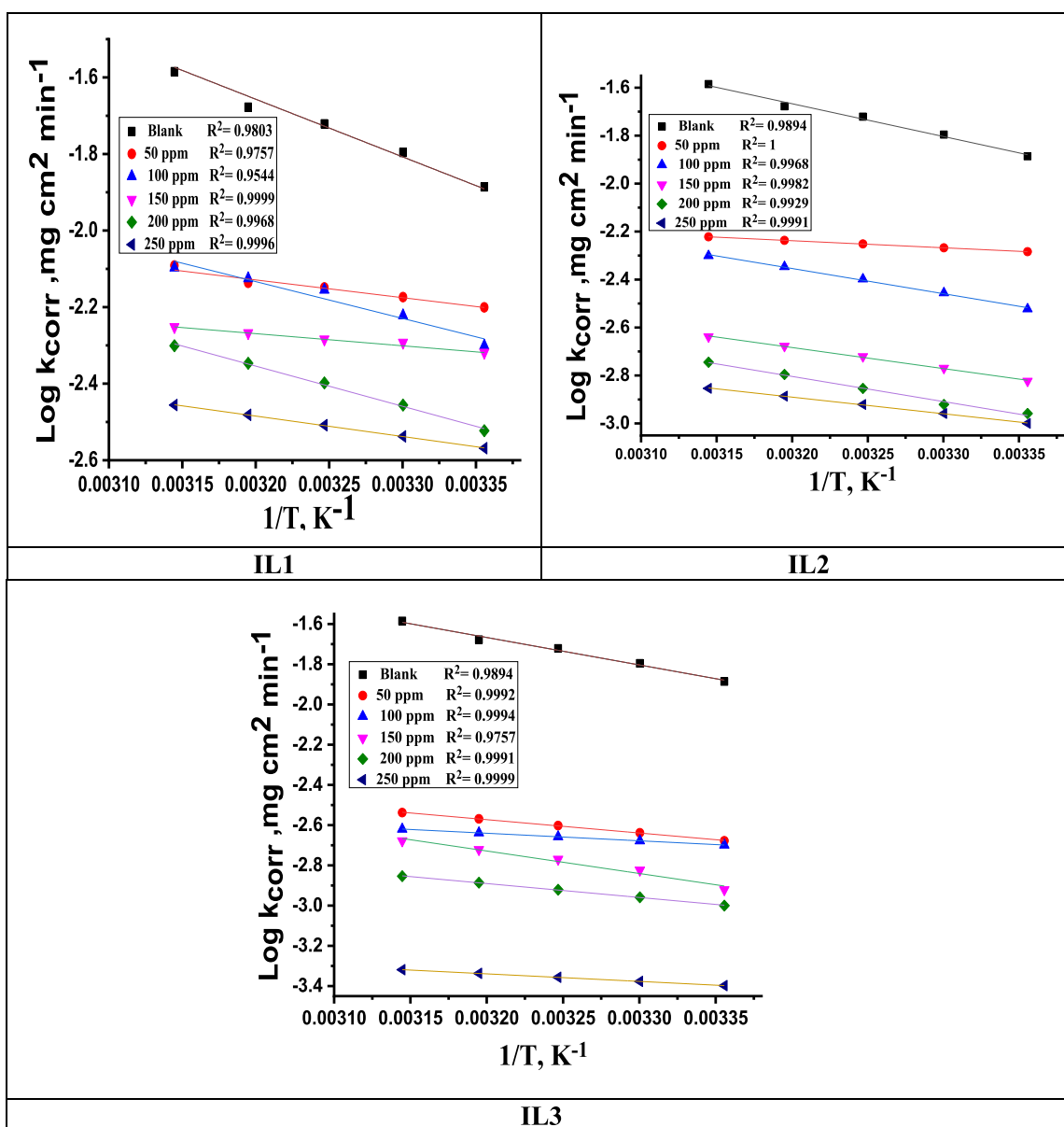


Figure 3. Graphs of  $\log k_{\text{corr}}$  vs  $1/T$  for investigated ILs.

substituting the N in the imidazolium ring increases the surface coverage.

**3.2.2. Effect of Temperature.** The influence of the temperature change on the corrosion rate of C-steel in 1 M HCl with and without the addition of varying IL concentrations (50–250 ppm) was studied at five different temperatures 298, 303, 308, 313, and 318 K. It turned out that  $k_{\text{corr}}$  decreases with increasing temperature, assuming that chemical adsorption was dominant at these conditions<sup>43</sup> and the IE % of IL3 at the highest temperature (318 K) reached 98.4%, indicating an exceptional capability of protection. The variation of IE % with temperature is shown in Figure 2, while the enumerated information is listed in Table 3.

**3.2.3. Thermodynamic Parameters.** The Arrhenius equation (eq 6) was implemented on the dissolute C-steel coupons in 1 M HCl with and without altered doses of ILs at various temperature (298–318 K) to learn about the activation energy ( $E_a^*$ ) of the transitional complex, which can be calculated from the slope of the  $\log k_{\text{corr}}$  versus  $1/T$  plot shown in<sup>44</sup> Figure 3,

and it was used in identifying the transition state (eq 7) to acquire both  $\Delta H^*$  and  $\Delta S^*$  from data earned from plotting  $\log(k_{\text{corr}}/T)$  versus  $1/T$ ,<sup>45</sup> as shown in Figure 4. With these parameters (displayed in Table 4), we can suggest the dominant type of adsorption of our inhibitors.

$$k_{\text{corr}} = A \exp\left(\frac{-E_a^*}{RT}\right) \quad (10)$$

$$k_{\text{corr}} = RT/Nh \exp\left(\frac{\Delta S^*}{R}\right) \exp\left(\frac{-\Delta H^*}{RT}\right) \quad (11)$$

where  $A$  is the Arrhenius pre-exponential factor,  $h$  is Planck's constant,  $N$  is Avogadro's number, and  $R$  is the universal gas constant. From the tabulated results, it turns out that the  $E_a^*$  is lowered by the addition of ILs in the solution, suggesting chemisorption of inhibitors on the metal surface as a result of stable metal–inhibitor complex formation. Also, the positive sign of enthalpy characterizes the reaction to be an endothermic one, which in turn demonstrates the chemisorption route. Addition of inhibitors exhibit a higher negative sign of entropy in the rate-determining step, which favors the

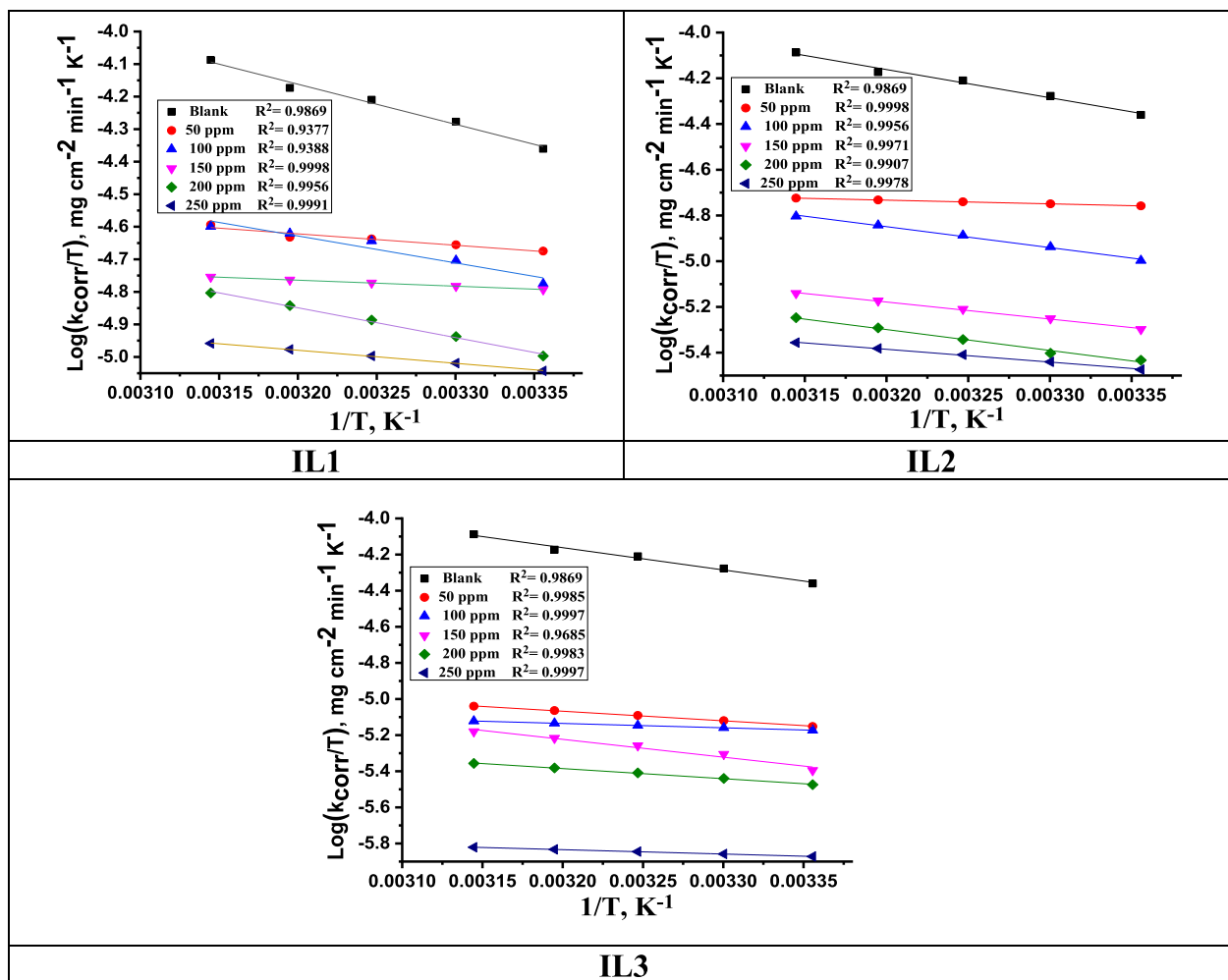


Figure 4. Plots of  $\log(k_{\text{corr}}/T)$  vs  $1/T$  for different concentrations of investigated ILs.

Table 4. Thermodynamic and Kinetic Parameters of ILs

compound	[Inh] ppm	$E_a^*$ kJ mol <sup>-1</sup>	$\Delta H^*$ kJ mol <sup>-1</sup>	$-\Delta S^*$ J mol <sup>-1</sup> K <sup>-1</sup>
blank	0.0	26.14	23.59	201.80
IL1	50	9.26	6.69	264.65
	100	18.41	15.85	235.48
	150	5.77	3.514	277.57
	200	20.08	17.53	23,435
	250	10.22	7.66	268.42
IL2	50	5.64	3.08	278.37
	100	20.08	17.53	234.35
	150	16.78	14.26	251.11
	200	20.04	17.48	243.11
	250	13.25	10.69	266.5
IL3	50	12.71	10.15	262.14
	100	7.18	4.62	281.12
	150	21.43	18.87	237.23
	200	13.25	10.69	266.51
	250	7.18	4.62	294.50

association over dissociation in the activated complex formation.<sup>46</sup> The results obtained verify the known thermodynamic relation between  $E_a^*$  and  $\Delta H^*$  characterizing the unimolecular reaction<sup>47</sup>

$$E_a^* - \Delta H^* = RT \quad (12)$$

The calculated value (2.56) is too close to that estimated in Table 4.

**3.2.4. Adsorption Isotherm.** Different adsorption isotherms are fitted graphically to characterize the adsorption. The adsorption was found to obey the Langmuir adsorption isotherm (Figure 5) with a correlation coefficient ( $R^2$ ) near to 1. Applying the Langmuir eq (eq 8) reflects the correlation between the surface coverage ( $\theta$ ) and the inhibitor equilibrium concentration ( $C$ ) in the bulk solution and assesses the adsorption equilibrium constant ( $K_{\text{ads}}$ ).

$$\frac{c}{e} = \frac{1}{K_{\text{ads}}} + C \quad (12a)$$

Then, we calculated the standard Gibbs free energy ( $\Delta G_{\text{ads}}^{\circ}$ ) from eq 13. By plotting  $\log K_{\text{ads}}$  vs  $1/T$  (Figure 6) eq 14 (van't Hoff eq), the standard enthalpy ( $\Delta H_{\text{ads}}^{\circ}$ ) was calculated from the slope of the lines. The standard entropy ( $\Delta S_{\text{ads}}^{\circ}$ ) can then be computed from eq 15.

$$\Delta G_{\text{ads}}^{\circ} = -RT \ln(55.5K_{\text{ads}}) \quad (13)$$

where  $R$  is the universal gas constant,  $T$  is the absolute temperature in K, and 55.5 refers to the water molar concentration.

$$K_{\text{ads}} = \Delta H_{\text{ads}}^{\circ} / 2.303RT + \text{constant} \quad (14)$$



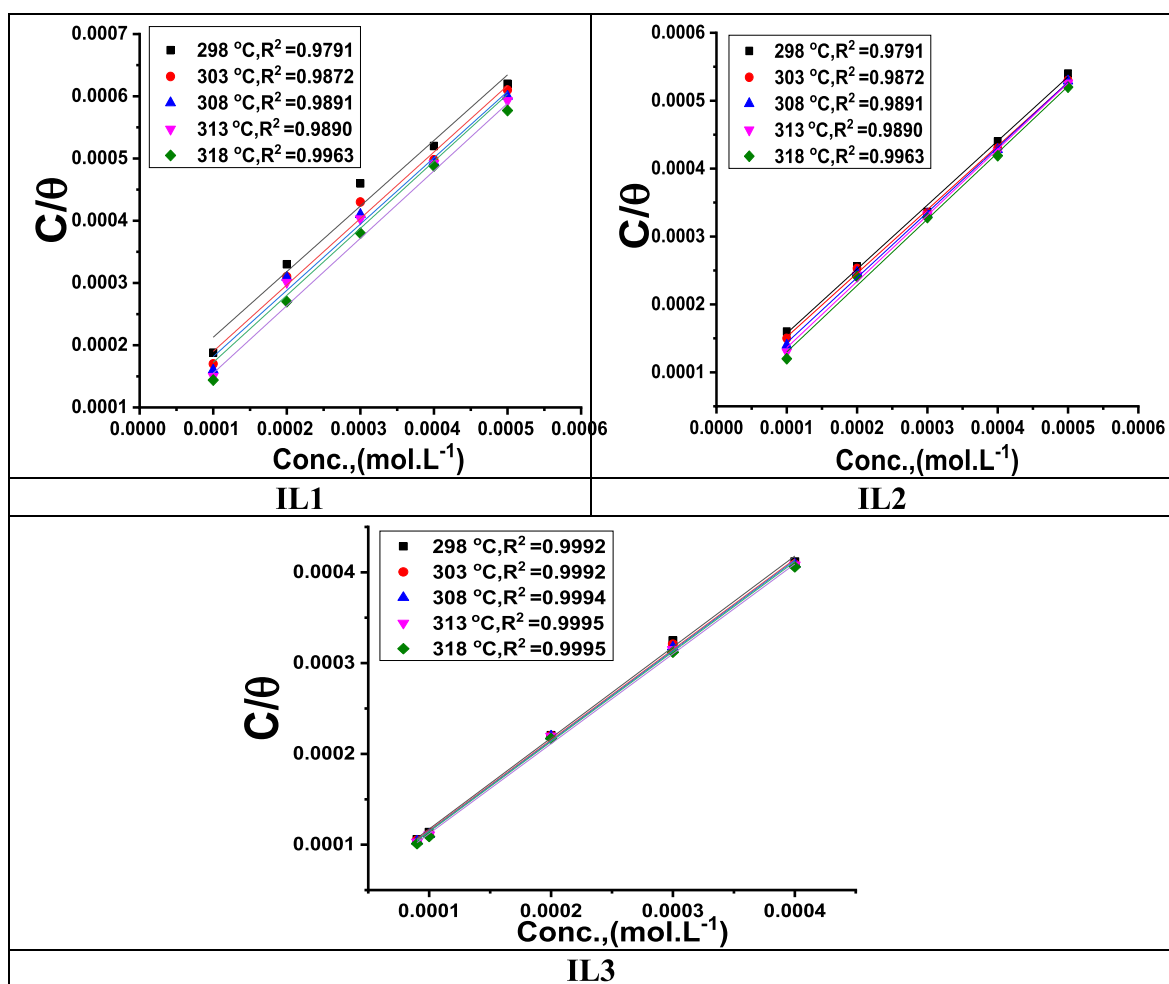


Figure 5.  $C/\theta$  versus  $C$  (Langmuir plots) for ILs at altered temperatures.

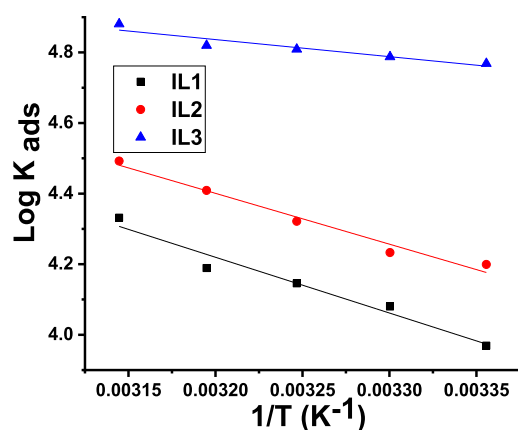


Figure 6. Plots of  $\log K_{\text{ads}}$  vs  $1/T$  for investigated ILs at different temperatures.

$$\Delta S_{\text{ads}}^{\circ} = (\Delta H_{\text{ads}}^{\circ} - \Delta G_{\text{ads}}^{\circ})/T \quad (15)$$

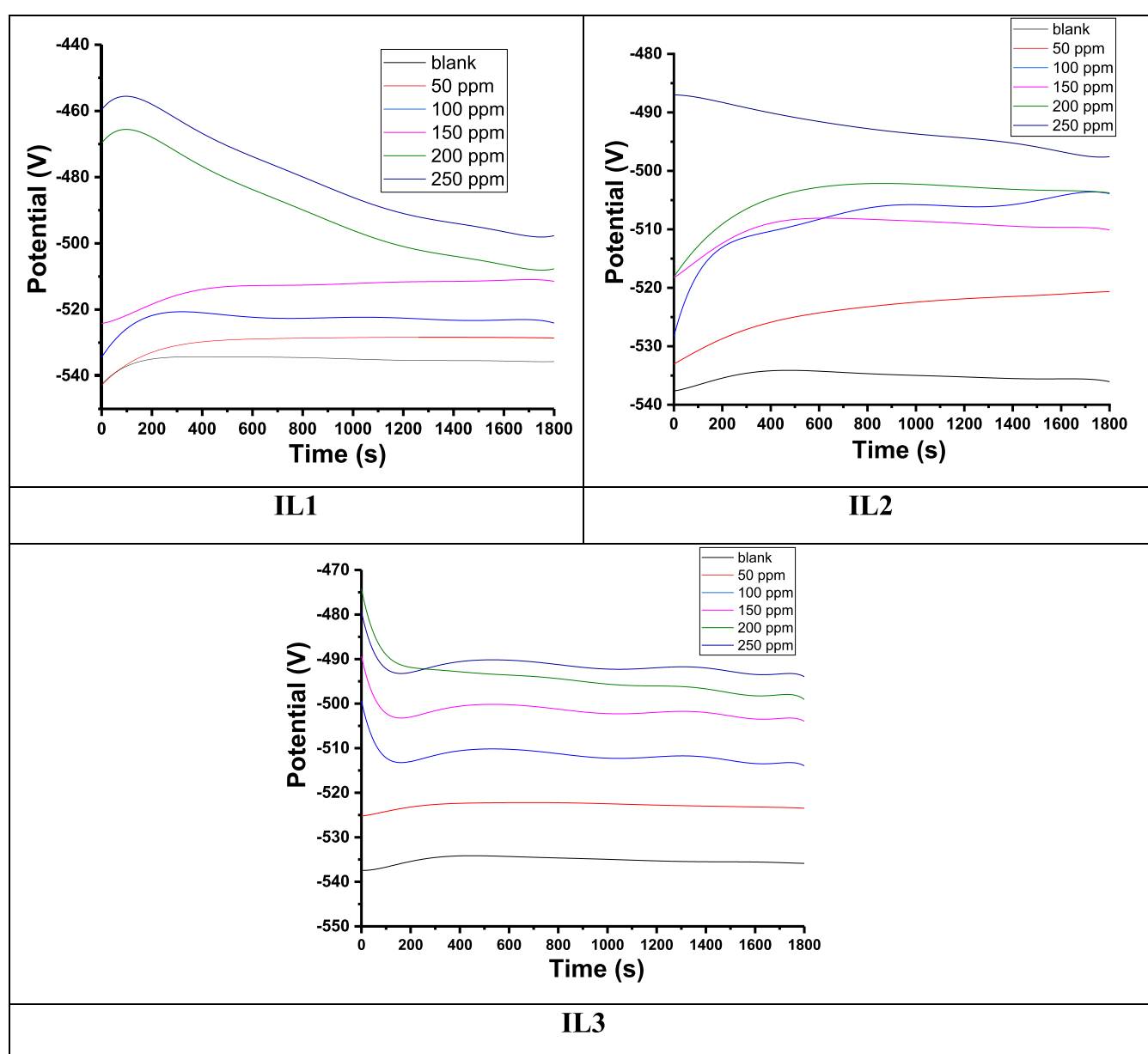
The computed results are listed in Table 5. From the tabulated results, we can find that  $\Delta G_{\text{ads}}^{\circ}$  has negative values, signifying that the adsorption can thermodynamically take place (spontaneous) and the stability of the adsorbed layer. According to the literature, when  $\Delta G_{\text{ads}}^{\circ}$  is less than or equal to  $-20 \text{ kJ mol}^{-1}$ , adsorption occurs by developing electrostatic attraction force between the inhibitor active center and

negatively charged metal surface (physisorption), while if  $\Delta G_{\text{ads}}^{\circ}$  exceeds  $-40 \text{ kJ mol}^{-1}$ , adsorption occurs by developing a coordination bond between the inhibitor and metal surface.<sup>48</sup> Our measurements show that the process involves both physisorption and chemisorption mechanisms (mixed type), with values ranging from  $-32$  to  $-40 \text{ kJ mol}^{-1}$ . The negative values of the  $\Delta G_{\text{ads}}^{\circ}$  parameter may be used to infer spontaneous adsorption and the stability of the adsorbent layer on C-steel externality.<sup>49</sup> Positive signs of  $\Delta H_{\text{ads}}^{\circ}$  ensure the endothermic reaction and thus chemisorption. The positive values of  $\Delta S_{\text{ads}}^{\circ}$  implies that randomness increases during adsorption operation.<sup>50</sup>  $K_{\text{ads}}$  values increase upon increasing the temperature, indicating the strength of the formed bond between inhibitor molecules and the d-orbital of iron.

**3.3. Electrochemical Measurements.** **3.3.1. Open Circuit Potential Measurements.** Figure 7 shows the open circuit potential (OCP) vs time curves for C-steel corrosion in 1.0 M HCl in the absence and presence of different concentrations of ILs (1–3) at 298 K. It is observed that the potential for uninhibited solution decreases with time. This phenomenon can be explained by the degradation of the C-steel with the formation of corrosive products on its surface. This phenomenon can be explained by the dissolution of the oxide film and the formation of a protective film on the metallic surface. From careful examination of the OCP curves, in inhibited solutions, it is observed that the potentials

Table 5. Thermodynamic Parameters of the Investigated ILs at Various Temperatures

inhibitors code	temperature K	$K_{ads}$ M <sup>-1</sup>	$-\Delta G^{\circ}_{ads}$ kJ mol <sup>-1</sup>	$\Delta H^{\circ}_{ads}$ kJ mol <sup>-1</sup>	$\Delta S^{\circ}_{ads}$ J mol <sup>-1</sup> K <sup>-1</sup>
IL1	298	9310	32.6	30.2	210.9
	303	12,019	33.8		211.4
	308	13,985	34.7		210.9
	313	15,455	35.6		210.4
	318	21,459	36.9		211.2
IL2	298	15,822	33.9	27.5	206.3
	303	17,094	34.7		205.5
	308	20,964	35.8		205.7
	313	25,641	36.9		206.1
	318	31,055	37.9		205.9
IL3	298	58,682	37.2	9.2	155.9
	303	61,271	37.9		155.7
	308	64,399	38.6		155.4
	313	66,021	39.3		155.2
	318	75,957	40.3		155.9

Figure 7. Variation of  $E_{OCP}$  vs time for C-steel in the 1.0 M HCl solutions in the absence and presence of altered doses of ILs (1–3) at 298 K.

**Table 6. Electrochemical Kinetic Parameters Concluded from Tafel Curves of the C-Steel Electrode in 1 M HCl with Various Concentrations of Investigated ILs at 298 K**

Inh	conc. ppm	$-E_{\text{corr}}$ mV vs SCE	$i_{\text{corr}}$ $\mu\text{A cm}^{-2}$	$\beta_a$ mV dec $^{-1}$	$-\beta_c$ mV dec $^{-1}$	$R_p$ $\Omega \text{ cm}^2$	$k_{\text{corr}}$ $\text{mmy}^{-1}$	$\theta$	IE %
blank	0.0	515	1316.7	193	189	55.0	15.39	—	—
IL1	50	551	570	202	176	72.5	6.669	0.567	56.7
	100	556	569	223	174	77.3	6.654	0.568	56.8
	150	529	469	189	184	99.9	5.490	0.644	64.4
	200	545	444	115	142	66.3	4.028	0.738	73.8
	250	531	246	122	144	101.5	2.875	0.813	81.3
IL2	50	517	837	133	177	72.3	9.786	0.365	36.5
	100	503	114	135	157	243.7	1.332	0.913	91.3
	150	493	103	116	116	194.4	1.206	0.922	92.2
	200	504	100	119	142	233.7	1.168	0.924	92.4
	250	492	86.5	115	157	275.5	1.011	0.934	93.4
IL3	50	499	100.1	111	132	235.9	1.711	0.924	92.4
	100	494	81.2	108	130	284.4	0.949	0.938	93.8
	150	485	70.5	79	166	275.1	0.824	0.946	94.6
	200	486	63.4	81	121	284.0	0.741	0.952	95.2
	250	488	48.2	86	154	425.0	0.564	0.963	96.3

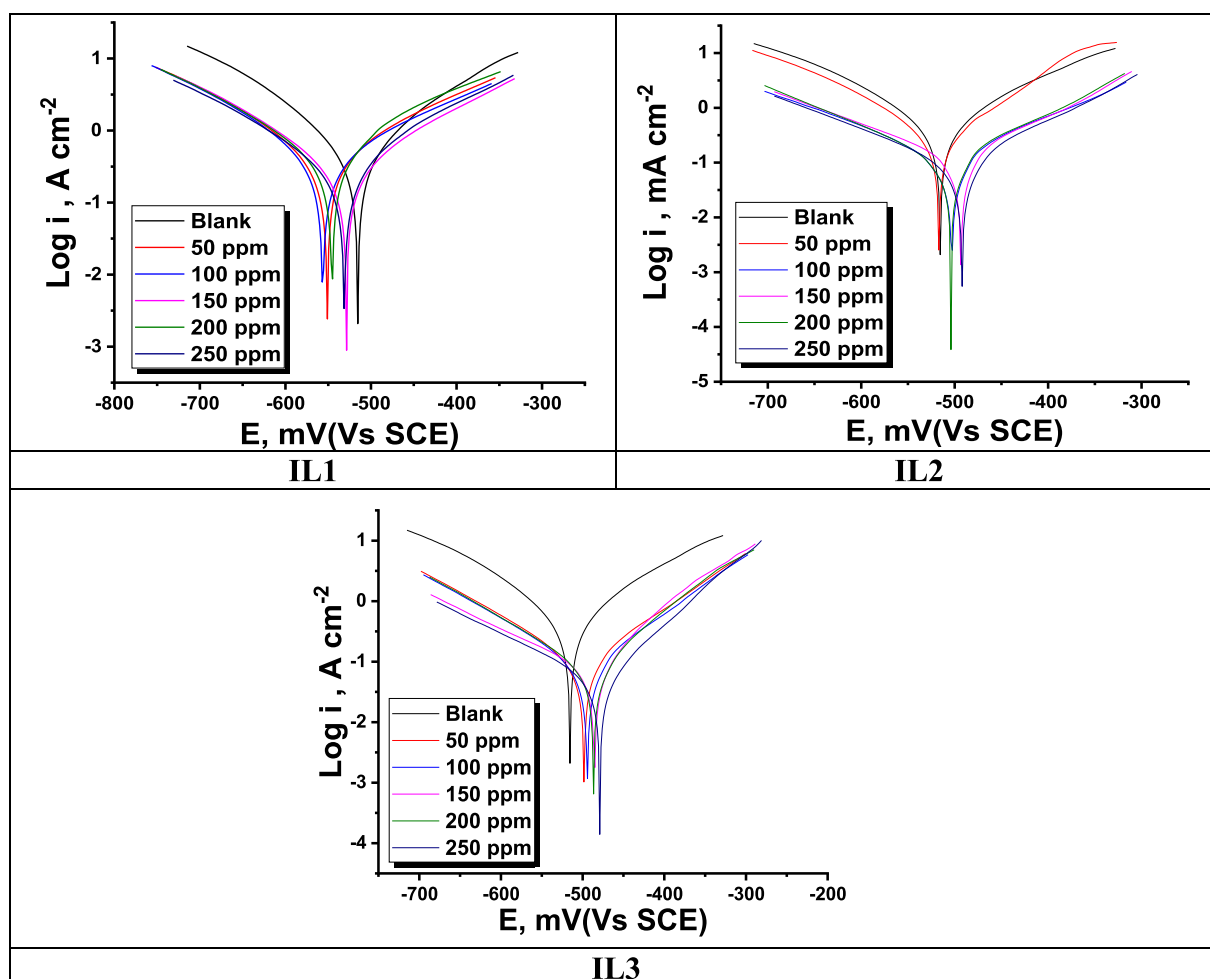


**Figure 8.** Tafel curves for C-steel in 1 M HCl with and without altered doses of ILs at 298 K.

obtained were shifted to values more positive than those obtained in uninhibited solutions.

**3.3.2. Potentiodynamic Polarization Tests.** PDP was performed in order to evaluate electrochemical kinetic parameters, which in turn give an indication about the type of inhibitors and to what extent they are efficient. The

evaluated kinetic parameters displayed in Table 6 which include the corrosion potential ( $E_{\text{corr}}$ ), corrosion current ( $i_{\text{corr}}$ ), Tafel cathodic and anodic slopes ( $\beta_c$  and  $\beta_a$ , respectively), corrosion resistance ( $k_{\text{corr}}$ ), and polarization resistance ( $R_p$ ), were recorded from plotting the Tafel curve ( $\log i_{\text{corr}}$ ,  $\text{mA cm}^{-2}$  vs  $E_{\text{corr}}$ ,  $\text{mV}_{\text{SCE}}$ ). Figure 8 displays the Tafel curves for the C-

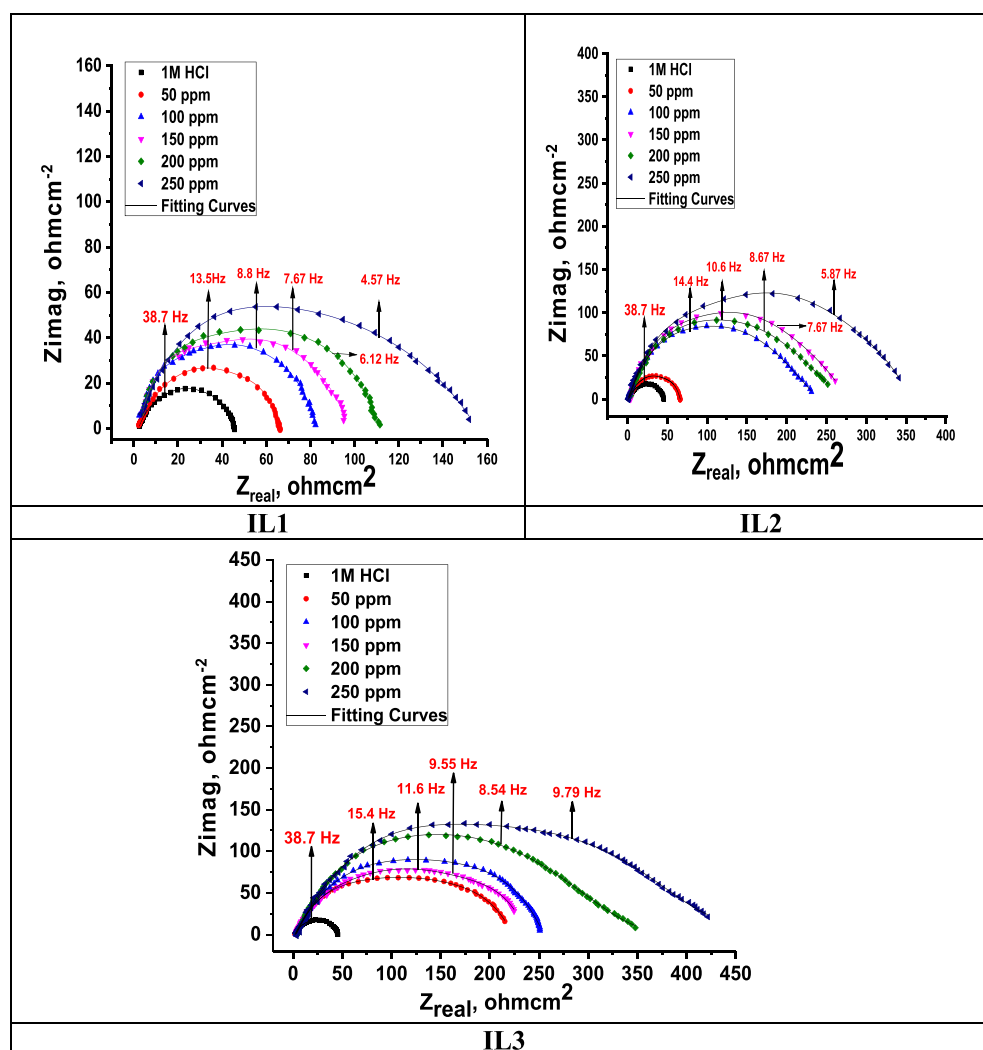


Figure 9. Nyquist graphs for C-steel in 1 M HCl at various concentrations of ILs at 298 K.

steel electrode in 1 M HCl with and without altered doses of used ILs. The addition of the ILs downshift the Tafel curves toward both cathodic and anodic sides with respect to the blank. The cathodic Tafel curves in Figure 8 yield parallel lines, suggesting that the hydrogen evolution is activation-controlled, and the reduction mechanism is not affected by the presence of ILs.<sup>51</sup> From the tabulated results, the change in  $E_{\text{corr}}$  before and after the addition of ILs does not exceed 85 mV, pointing to a mixed type inhibitor.<sup>52</sup> The anodic and cathodic Tafel slopes ( $\beta_c$  and  $\beta_a$ ) values are not affected significantly by the addition of ILs compared to those of the blank. As a result, the addition of ILs restricted the active sites of the electrode surface, reducing the amount of surface accessible for corrosion reactions and demonstrating the mixed kind of inhibitors,<sup>53</sup> while taking into account that the anodic mechanism is more severely impacted. In the present study,  $E_{\text{corr}}$  values in the presence of ILs move toward the cathodic side with respect to the blank, and the range of shifting is 56–43 mV, which suggests that ILs acted as a mixed type of inhibitor but predominantly the cathodic type.<sup>53</sup> The decrease in  $i_{\text{corr}}$  and the increases of  $R_p$  and  $\theta$  with the increase of inhibitor concentrations substantiate their inhibitory impact, where IE % can be calculated from eq 2. The experimental findings of Tafel

curves were in good agreement with the data obtained in the case of the WL method.

3.3.3. *Electrochemical Impedance Spectroscopy Technique.* EIS may be used to monitor the kinetics of the electrode processes and the surface characteristics of the systems under investigation. Figure 9 shows Nyquist plots for C-steel in 1 M HCl in the presence and absence of altered doses of utilized ILs. Figure 9 has a single semicircle at high frequency, which indicates the charge transfer of the corrosion process. Bode charts for the identical ILs are shown in Figure 10. The single peak shown in all the employed ILs' Bode graphs demonstrated the existence of a single time constant, as indicated by the Nyquist plot. An electrical circuit was utilized to fit all EIS spectra to get a quantitative description of the corrosion system.<sup>54</sup> Based on the equivalent circuit (Figure 11),  $R_s$  denotes the solution resistance,  $R_{ct}$  is the charge transfer resistance and  $C_{dl}$ , double layer, which usually behaves as a constant phase element CPE rather than as a pure capacitor. The Nyquist graph shows semicircular curves whose diameter increases with the increasing concentration until reaching the optimum concentration (250 ppm), which increases the impedance magnitude as well as shifts the phase angle to a higher value, and this demonstrates the adsorption of ILs on the C-steel surface.<sup>55</sup> The diameter of the

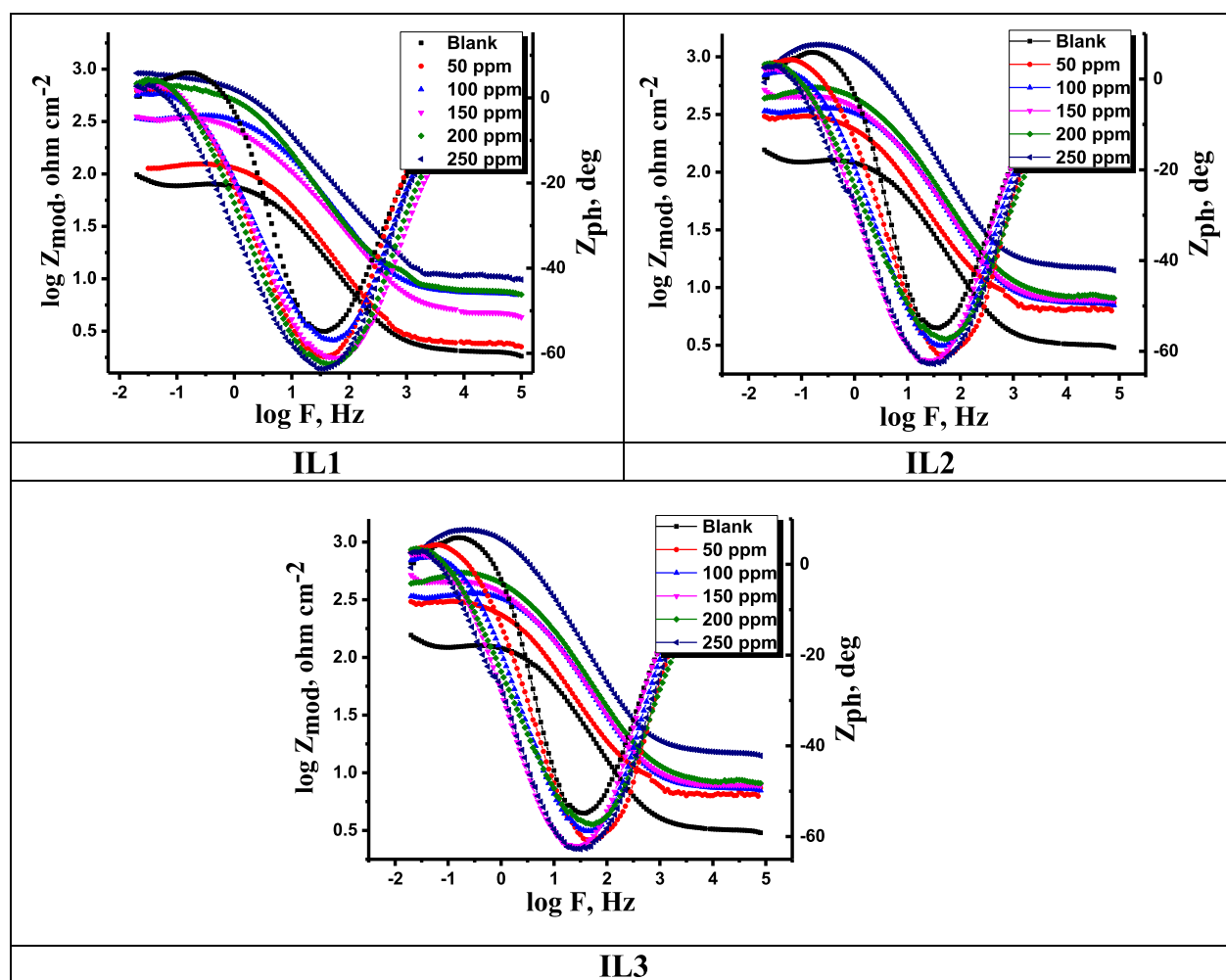


Figure 10. Bode graphs for C-steel in 1 M HCl at various concentrations of ILs at 298 K.

Table 7. EIS Data for Corrosion of C-Steel without and with Altered Concentrations of ILs at 298 K

inhibitor	conc., ppm	$R_{ct}$ , $\Omega$ cm <sup>2</sup>	$R_p$ , $\Omega$ cm <sup>2</sup>	$C_{dl}$ , $\mu$ F cm <sup>-2</sup>	$\theta$	IE %	goodness of fit ( $\chi^2$ )
blank		43.3	55.0	462			$17.47 \times 10^{-3}$
IL1	150	73.2	92.9	392	0.408	40.8	$22.54 \times 10^{-3}$
	100	88.2	112.0	260	0.509	50.9	$21.55 \times 10^{-3}$
	150	92.1	117.0	210	0.530	53.0	$19.14 \times 10^{-3}$
	200	120.6	153.1	150	0.641	64.1	$19.24 \times 10^{-3}$
	250	160.1	203.7	110	0.730	73.0	$20.45 \times 10^{-3}$
IL2	50	75.8	96.3	383	0.429	42.9	$22.45 \times 10^{-3}$
	100	229.1	291.0	69	0.811	81.1	$21.47 \times 10^{-3}$
	150	242.6	308.9	52	0.822	82.2	$18.54 \times 10^{-3}$
	200	257.2	327.3	77	0.832	83.2	$22.15 \times 10^{-3}$
	250	370.6	329.3	58	0.883	88.3	$20.88 \times 10^{-3}$
IL3	50	235.2	298.9	75	0.816	81.6	$23.43 \times 10^{-3}$
	100	275.5	350.25	60	0.843	84.3	$18.47 \times 10^{-3}$
	150	296.5	376.6	57	0.854	85.4	$20.54 \times 10^{-3}$
	200	382.1	486.64	48	0.887	88.7	$23.57 \times 10^{-3}$
	250	432.3	549.9	46	0.900	90.0	$21.87 \times 10^{-3}$

semicircle of the studied ILs increased in the following order IL3 > IL2 > IL1. The impedance spectrum is not a perfect semicircle, has a center depression that lies below the real axis, and mimics depressed capacitive loops. This behavior frequently relates to surface heterogeneity, which can be caused by surface roughness, dislocations, the distribution of

active sites, or the adsorption of inhibitor molecules.<sup>56</sup> Figure 9 makes evident that the experimental and theoretical curves are well-fitted. The assessed values for ( $\chi^2$ ) in Table 7 provide evidence for the use of an analogous circuit and a fitting of high quality. This also proves that the control of corrosion is essentially done by the charge transfer process.<sup>57</sup> From the

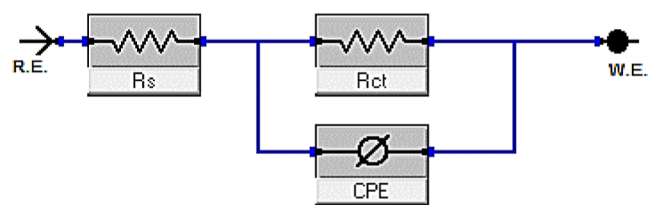


Figure 11. Electrical circuit utilized to fit the EIS data.

Table 8. Tabulating the Roughness Values of Free C-Steel, Corroded C-Steel, and C-Steel Protected by IL1, IL2, and IL3

specimen	roughness Sa (nm)
free C-steel coupons	50.481 nm
corroded CS coupons	349.23 nm
C-steel inhibited by IL1	184.27 nm
C-steel inhibited by IL2	160.8 nm
C-steel inhibited by IL3	152.59 nm

data in Table 7, it can be seen that the capacitance of the double layer ( $C_{dl}$ ) decreases. The double layer capacitance ( $C_{dl}$ ) values can be calculated by incorporating the CPE parameter values  $Y$  and  $n$  in eq 9<sup>58</sup>

$$C_{dl} = Y_0^{(n-1)} / \sin(n(\pi/2)) \quad (16)$$

where  $Y_0$  is the angular frequency ( $\omega = 2\pi f_{max}$ ) at which the imaginary part of the impedance ( $-Z_{im}$ ) is maximal and  $n$  is the phase shift, which can be used as a gauge of the heterogeneity or roughness of the C-steel surface.

The  $C_{dl}$  at the frequency  $f_{max}$ , where the imaginary component of the impedance spectrum is the greatest, was determined using eq 17<sup>59</sup>

$$C_{dl} = (1/2\pi f_{max} R_{ct}) \quad (17)$$

The Helmholtz model predicts that this phenomenon is caused by either an increase in the electrical double layer thickness or a drop in the local dielectric constant<sup>60</sup>

$$C_{dl} = A\epsilon\epsilon_0/\delta \quad (18)$$

where  $\epsilon$  is the dielectric constant of the medium,  $\epsilon_0$  is the vacuum permittivity,  $A$  is the electrode area, and  $\delta$  is the thickness of the protective layer. The charge transfer resistance ( $R_{ct}$ ) increases as the concentration of ILs improves due to the increase in the thickness of the protective layer,<sup>61</sup> which means a higher IE % (calculated from eq 3). The IE % is arranged in the order IL3 > IL2 > IL1, which is in agreement with WL and PDP methods.

**3.4. Surface Examination.** **3.4.1. Fourier Transform Infrared Spectroscopy.** Our newly synthesized ILs were characterized by using FTIR spectroscopy, and an explanation has been introduced before, so we repeated the FTIR analysis

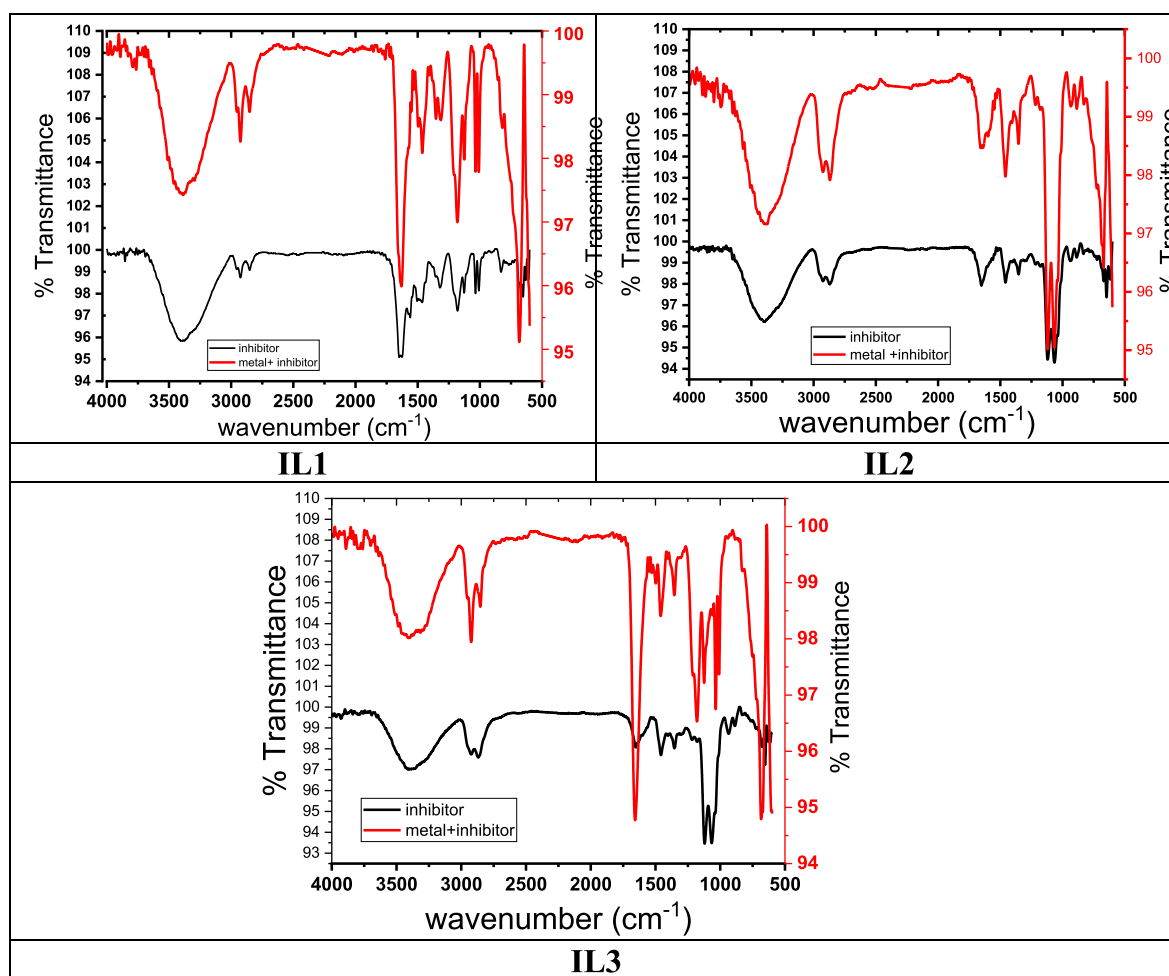
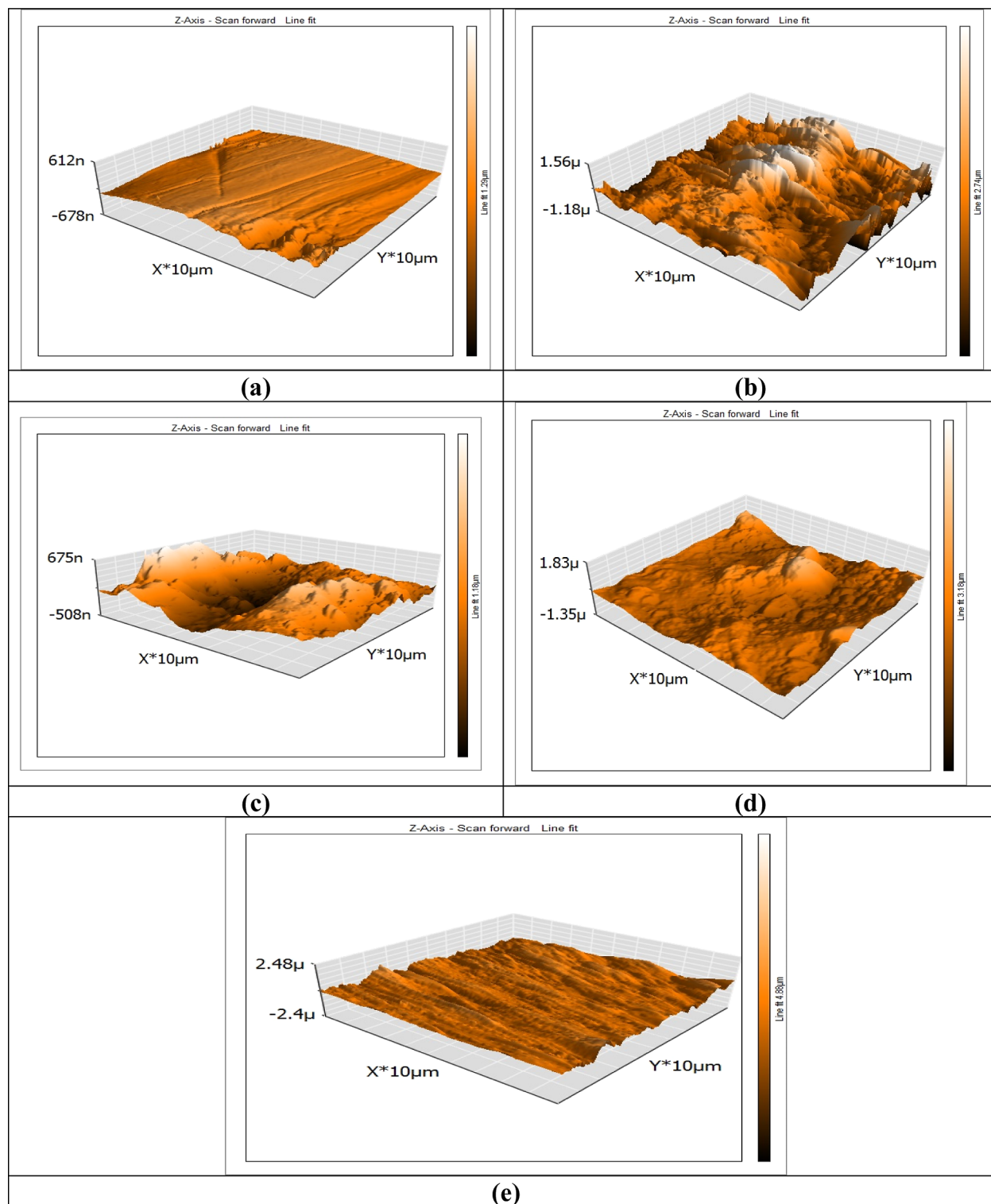


Figure 12. Double plot of FTIR spectra of both free ILs and ILs adsorbed on C-steel sheets.



**Figure 13.** AFM scan for free C-steel coupons (a), attacked C-steel coupons (in HCl only) (b), protected C-steel coupons with IL3 (c), protected C-steel coupons with IL2 (d), and protected C-steel coupons with IL1 (e).

on C-steel coupons that were immersed in 1 M HCl acid with the optimum concentration (250 ppm) of ILs. The obtained spectrum turned out to be approximately identical to that of the free inhibitor with some moves being detected in the spectra, which may be attributed to the interaction between ILs and the C-steel surface, giving absolute evidence of the inhibitor adsorption on the metal surface resulting in corrosion protection.<sup>62</sup> In Figure 12 which displays a comparison

between FTIR spectra of ILs in free and adsorptive states, it is easy to figure out functional groups of the ILs on the metal surface such as the CH...H<sub>2</sub>O broad band, C–N sharp band, aromatic C–C and C=C, and aliphatic C–H.

**3.4.2. Atomic Force Microscopy Analysis.** Mean roughness ( $S_a$ ) values have a significant role in the recognition of the inhibitor efficiency.<sup>63</sup> AFM scanning was performed on five C-steel coupons with the scan area equal to  $10 \times 10 \mu\text{m}^2$  and

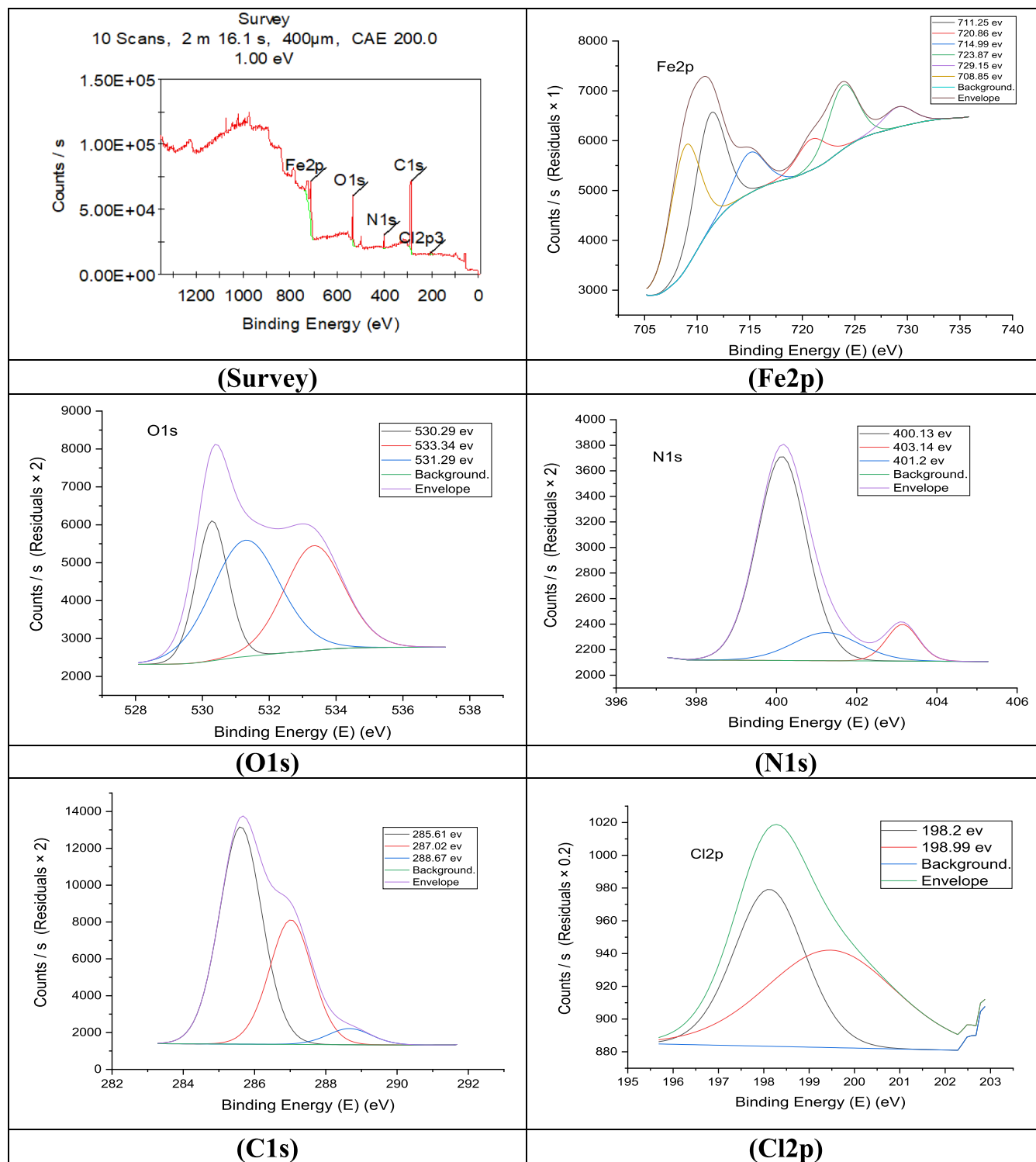


**Figure 14.** Photoelectric X-rays results from survey, Fe 2p, O 1s, N 1s, C 1s, and Cl 2p at 1 M hydrochloric acid solution with 250 ppm IL3.

data points numbering  $256 \times 256$  at a scan rate equal to 1 Hz. The atomic force microscope was operated in the contact mode using a nonconductive silicon probe using nanosurf C300 (version 3.5.0.31) software. The first coupon is a free polished C-steel, the second one is C-steel immersed in 1 M HCl for 24 h (corroded C-steel coupons), and the third one is C-steel immersed in 1 M HCl with the addition of 250 ppm IL1 for 24 h (inhibited C-steel), with the last 2 coupons inhibited by IL2 and IL3. The results are given in Table 8.

The tabulated results give a solid connotation of the inhibitory capability of the inhibitors,<sup>64</sup> also confirming the efficiency according to the following arrangement IL3 > IL2 > IL1, which is in line with the WL method and electrochemical experiments. Figure 13 shows the scans of free C-steel (a), corroded C-steel in HCl (b), C-steel inhibited by IL3(c), C-steel inhibited by IL2(d), and C-steel inhibited by IL1(e).

**3.4.3. X-ray Photoelectron Spectroscopy.** High-resolution XPS spectroscopy became vital in qualitative and quantitative



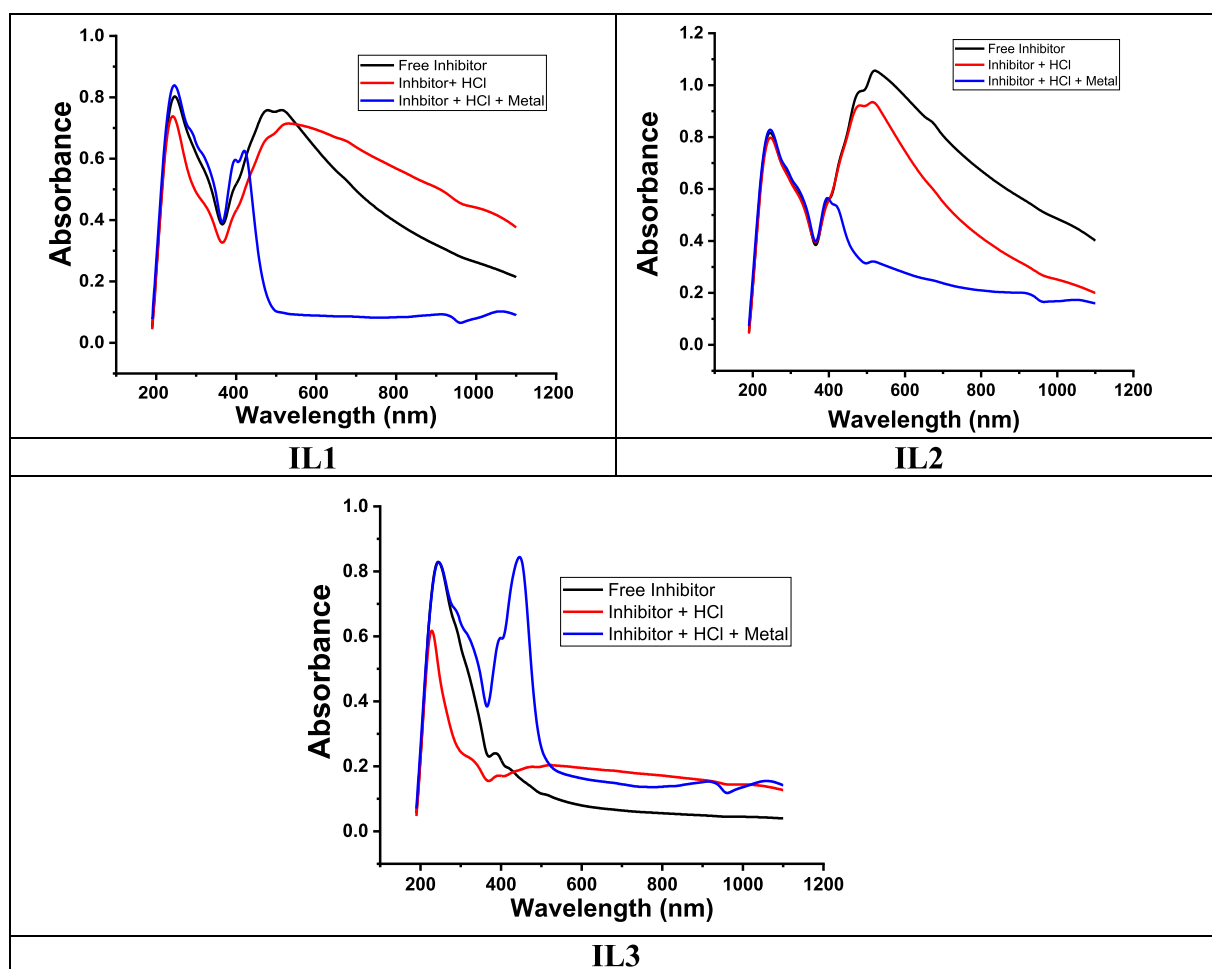


**Figure 15.** UV–vis spectra of free IL3, IL3 + HCl, and IL3 + HCl + C-steel at 298 K.

analysis of the identified species at the metal/inhibitor interaction. Figure 14 displays the photoelectric X-ray results from survey, Fe 2p, O 1s, N 1s, C 1s, and Cl 2p at 1 M hydrochloric acid solution with 250 ppm IL3. The XPS spectrum of Fe 2p splits into six peaks: 708.85 eV was attributed to metallic iron<sup>65</sup> and 711.25 eV and 714.99 eV referred to Fe<sub>2</sub>O<sub>3</sub> and Fe(OH)<sub>3</sub>, respectively[64], while peaks present at 723.87 and 729.88 eV were attributed to Fe 2p<sub>1/2</sub> via Fe<sub>3</sub>O<sub>4</sub>,  $\alpha$ -Fe<sub>2</sub>O<sub>3</sub>, and FeOOH<sup>66</sup> and 729.15 eV referred to oxidation at the carbon steel surface. On studying the XPS spectrum of C 1s, we found three peaks: two at 285.61 eV and 287.02 eV attributed to C–C and C–O, respectively, and a peak at 288.87 eV referring to C=O.<sup>67</sup> Looking at the O 1s spectrum, the peak at 530.29 eV refers to metal oxide and that at 531.29 eV refers to O–H. Studying N 1s peaks is the most essential as having a peak at 401.2 eV attributed to coordination N in the imidazole ring strongly suggests the adsorption of the IL inhibitors at the C-steel surface<sup>68</sup> as well as the two peaks of Cl 2p appearing at 198.2 and 198.99 eV indicating the interaction of chloride anions with the substrate.<sup>69</sup> Finally, we conclude that XPS firmly approves the ability of our synthesized inhibitors on the carbon steel surface.

### 3.5. Test Solution Analysis. 3.5.1. UV–Vis Spectroscopy.

UV–vis spectroscopy was carried out on three solutions, the first containing only the stock solution of our newly synthesized inhibitors, the second one containing the inhibitor

stock solutions and corrosive medium (HCl), and the last one containing the stock solution + HCl + carbon steel immersed in it. The obtained curves are displayed in Figure 15, where we found that the significant peak in the case of the free stock solution is at 240 cm<sup>-1</sup> and the peak after the addition of HCl is at 226 cm<sup>-1</sup>. The insignificant change in the wavenumber suggests the high stability of the inhibitors. After the immersion of C-steel coupons, the peaks are shifted to 441 cm<sup>-1</sup>, attributed to intramolecular charge transfer,<sup>70</sup> suggesting the formation of a metal–inhibitor complex, which also demonstrates our preceding results, and it also suggests that the inhibition of the inhibitors may follow a mainly chemisorption route.

**3.6. Theoretical Modeling. 3.6.1. Density Functional Theory.** The optimized geometrical structures, highest occupied molecular orbital (HOMO), and lowest unoccupied molecular orbital (LUMO) are illustrated in figures collected in Table 9 and their related chemical quantum descriptors are stated in Table 10. According to the frontier molecular orbital theory (FMO),  $E_{\text{HOMO}}$  and  $E_{\text{LUMO}}$  values describe the acceptance or donation proficiency of the inhibitors molecules at the metal–inhibitor interface.<sup>71</sup> Subsequently, the growth in  $E_{\text{HOMO}}$  values and the reduction in  $E_{\text{LUMO}}$  values boost the inhibition capability,<sup>72</sup> and as a result, the molecules with a lower energy gap ( $\Delta E$ ) are assigned to have higher tendency toward adsorption because it indicates that only a small energy is needed for the electron transition from  $E_{\text{HOMO}}$  to  $E_{\text{LUMO}}$ .<sup>73</sup>

Table 9. Figures of Optimized Structures, HOMO, and LUMO

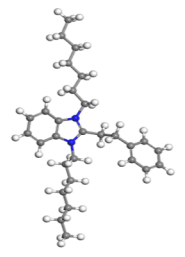
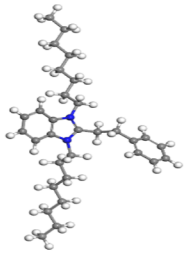
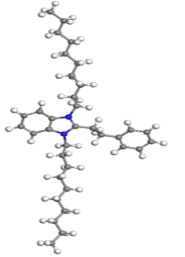
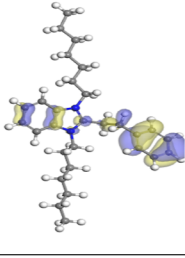
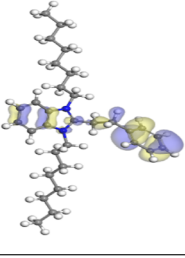
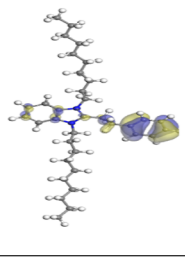
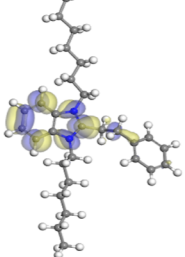
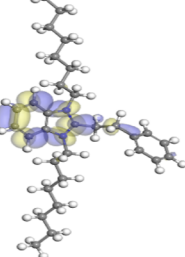
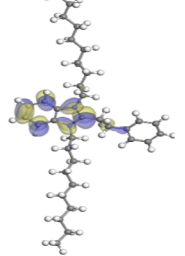
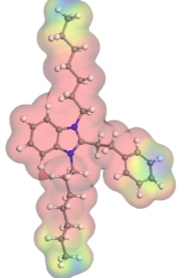
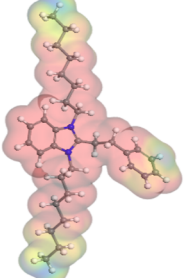
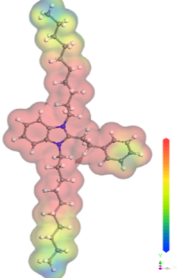
	IL1	IL2	IL3
Optimized structure			
HOMO			
LUMO			
MEP			

Table 10. Displaying Parameters Related to DFT

quantum parameters	IL1	IL2	IL3
$E_{\text{HOMO}}$ , eV	-5.894	-5.874	-5.869
$E_{\text{LUMO}}$ , eV	-2.103	-2.121	-2.127
$\Delta E$ , eV	3.79	3.75	3.74
$I$	5.89	5.87	5.87
$A$	2.10	2.12	2.13
$\chi$	4.00	4.00	3.99
$\eta$	1.90	1.88	1.87
$\sigma$	0.53	0.53	0.53
$\omega$	4.22	4.26	4.27
$\Delta N$	0.79	0.795	0.80
$\Delta E_{\text{back-donation}}$	-0.47	-0.47	-0.47
dipole moment, Debye	1.5343	2.1179	6.0452
molecular surface area, $\text{\AA}^2$	512.993353	553.669358	630.645541

From our tabulates results,  $\Delta E$  values are 3.79, 3.75, and 3.74 for IL1, IL2, and IL3, respectively, which demonstrates that

IL3 has the lowest value among them so as to have the highest inhibition impact. In Table 9, the figures illustrating the geometrical structures show that the HOMO is localized at the  $\text{Cl}^-$  anion, representing it as the desired site for the electrophilic attack. The values of electronegativity ( $\chi$ ) also give an indication about the inhibition efficiency as the donation reactivity increases with lower electronegativity values.<sup>74</sup> The electronegativity of IL3 is 3.99 lower than that of IL2 and IL1, which proves our experimental results. The stability and the inhibitors undergo chemical change are confirmed by hardness ( $\eta$ ) and softness ( $\delta$ ), and it is known that as the softness increases and hardness decreases this affirms the high reactivity and this is attributed to the fluent donation of electrons from the inhibitors to the carbon steel surface.<sup>75</sup> Our inhibitors recorded softness values of 0.53, 0.53, and 0.53 and hardness values of 1.90, 1.88, and 1.87 for IL1, IL2, and IL3, respectively, which indicates that IL3 is the one among them with the easiest electron transition.  $\Delta N$  describes

Table 11. Final Equilibrium configuration Obtained from Monte Carlo Simulation

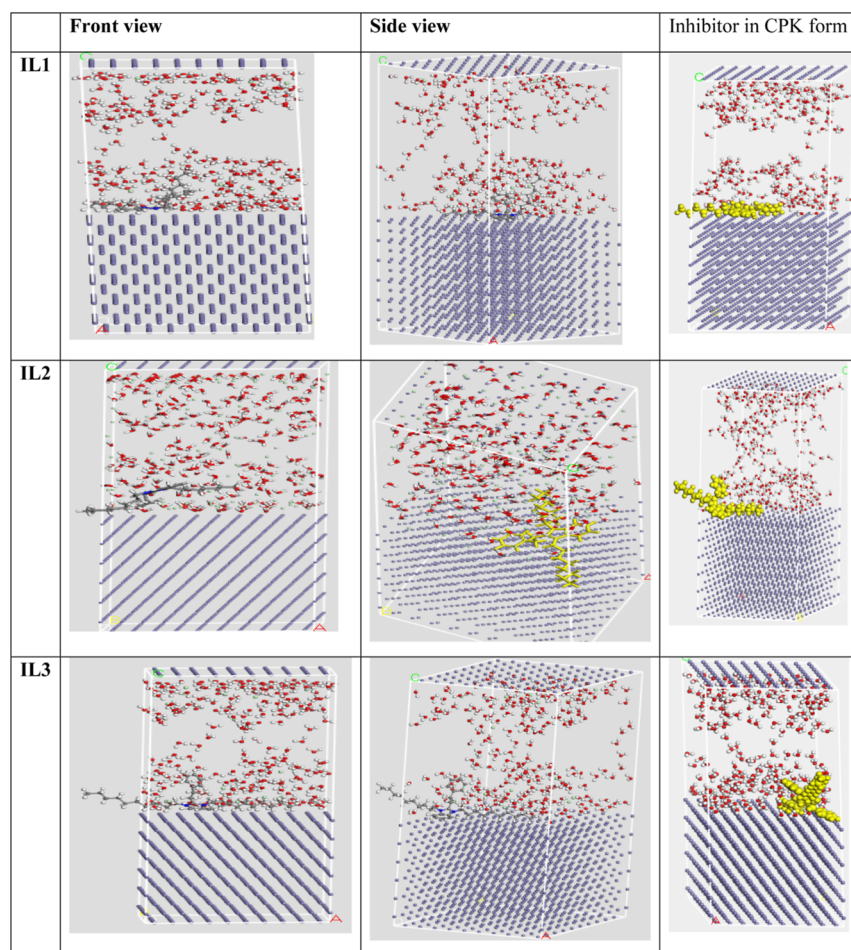


Table 12. Related Parameters Obtained from Monte Carlo Simulation

structures	adsorption energy	rigid adsorption energy	deformation energy	$dE_{\text{ads}}/dN_i$	$dE_{\text{ads}}/dN_i$
Fe(1 1 0) IL1 water	-3270.779	-3433.918	163.13	-253.19	-7.27
Fe(1 1 0) IL2 water	-3882.259	-4057.191	174.93	-234.80	-8.16
Fe(1 1 0) IL3 water	-4148.334	-4333.033	184.69	-307.35	-9.38

the ability of molecules in granting electrons, so as tabulated, IL3 has the highest  $\Delta N$ , equaling 0.80; therefore, it has the highest electron contributing competency.<sup>76</sup> When  $\Delta E_{\text{back-donation}}$  is lower than zero, this means that the transferred electrons will be back-donated, which shows the most energetic inhibitory capacitance assigned to high electron contribution.<sup>77</sup> One of the most crucial parameters to be a strong indicator of the inhibition pathway is the dipole moment.<sup>78</sup> The inhibition efficiency increases with the increasing dipole moment as a result of deformation energy enhancement. The dipole moment values of IL1, IL2, and IL3 are 1.5343, 2.1179, and 6.0452 D, respectively, which gives clear evidence that IL3 is the most efficient inhibitor in this series. There is a strong association between the surface area and the ability of ILs in defending the carbon steel surface,

where a greater molecular surface area exhibits higher protection. By investigating the surface area of our compounds, we find that IL3 is the largest one with a value of 630.645541  $\text{Å}^2$ , which makes it the best inhibitor of the series, followed by IL2 with a value of 553.669358  $\text{Å}^2$  and then IL1 with a value 512.993353  $\text{Å}^2$ .

Molecular electrostatic mapping (MEP) (Table 9) give a visual description about the local reactivity (the most preferred molecular adsorption sites)<sup>79</sup> based on the general charge distribution<sup>80</sup> where the atoms with the highest negative charge (red region) are presumed as nucleophilic centers (electron donors),<sup>81</sup> but atoms with the biggest positive area (blue region) are presumed as electrophilic centers.<sup>82</sup> Therefore, atomic nitrogen in the imidazole ring representing the red region is the highest contributor in the nucleophilic attack and

is the proper one in the interaction with the C-steel surface. The nucleophilic attack (red region) which is the proper in the interaction with C-steel surface.

**3.6.2. Monte Carlo Stimulation.** Monte Carlo simulation was performed to get the idea of adsorption strength and the stable configuration arrangement of investigated ILs on the C-steel facet. Stimulation was done by the adsorption lactor module to detect the interaction between ILs and the surface area of the Fe (1 1 0) crystal along with discovering the best adsorption sites.<sup>83</sup> Table 11 displays the adsorption configuration, which is nearly parallel in position, which in turn increases the surface coverage and inhibition efficiency.<sup>84</sup> The descriptors computed from Monte Carlo stimulation are given in Table 12. The tabulated adsorption energies are  $-3270.779$ ,  $-3882.259$ , and  $-4148.334$  kcal/mol for IL1, IL2, and IL3, respectively. The output shows that the three inhibitors are efficient adsorptive inhibitors taking into account that the better one is IL3, which is in agreement with the experimental results.<sup>85</sup> Rigid adsorption energies are  $-3433.918$  (IL1),  $-4057.191$  (IL2), and  $-4333.033$  (IL3) kcal/mol, where Inh3 is the most negative, while the deformation energies are  $163.13$  (IL1),  $174.63$  (IL2), and  $184.69$  (IL3) kcal mol<sup>-1</sup>; also, IL3 has the highest value, which confirms the greater inhibitory impact of IL3 compared to that of IL2 and IL1.  $dE_{ad}/dN_i$  provides information about the metal adsorbents as if they are adsorbed or neglected,<sup>86</sup> so when comparing  $dE_{ad}/dN_i$  for inhibitors ( $-253.19$ ,  $-234.80$ , and  $-307.35$  kcal mol<sup>-1</sup>) and  $dE_{ad}/dN_i$  for water ( $-7.27$ ,  $-8.16$ , and  $-9.38$  kcal mol<sup>-1</sup>), it is found that the values in the case of water are very low compared to that of the inhibitors, proving the replacement of water molecules by inhibitor molecules. Based on theoretical modeling, it is obvious that ILs based on benzimidazole chloride derivatives proved to be powerful inhibitors for the carbon steel, which is confirmed by experimental and spectral investigation.

**3.7. Corrosion Inhibition Mechanism.** The use of ILs as corrosion inhibitors is considered an excellent approach to green chemistry due to the properties of the inhibitors like solubility in water with no need of toxic solvents, low cost, and chemical and thermal stability.<sup>87</sup> It is not possible to categorize the adsorption of organic molecules on solid surfaces as primarily physical or chemical. This is how it may be explained



- (i) Free electron pairs of heteroatoms and electrons of numerous bonds, as well as the phenyl group and unoccupied d-orbitals of iron, interact as donors and acceptors in chemical adsorption of ILs.<sup>88,89</sup>
- (ii) Physical adsorption between the charged C-steel surface and the charged inhibitor molecules (ILs) can also help the inhibitor molecules (ILs) adhere to the surface of the C-steel. According to the following equation, ILs in HCl are in a protonated state that is in equilibrium with the equivalent neutral form:

Due to specific adsorption and the low degree of hydration of chloride ions, they should initially be adsorbed on the positively charged metal surface. More cations are attracted to the metal's solution side due to the additional negative charge produced by chloride ion adsorption. The negatively charged C-steel surface and positively charged  $[IL H]^+$  are electrostatically attracted to one another, whereupon the IL molecules adsorb and create a barrier. At the cathodic sites of C-steel, the

protonated ILs are additionally adsorbed in opposition to hydrogen ions that decrease to H<sub>2</sub> gas.<sup>90,91</sup>

- (iii) An electron from Fe's d orbital might be moved to an open IL molecule's  $\pi^*$  (antibonding) orbital in order to remove the additional negative charge from the C-steel. This would increase adsorption on the C-steel surface.

## 4. CONCLUSIONS

- Results obtained qualified that ILs tested are an efficient inhibitor.
- The inhibiting effect increased with the IL concentration to attain the maximum inhibitory effect order of IL3 (98.4%) > IL2 (96.1%) > IL1 (86.6%) at 250 ppm, 318 K
- At elevated temperature, the IE % increased with the decrease of the activation energy.
- ILs acted according to the Langmuir adsorption isotherm model and the negative of Gibb's free energy is a sign of spontaneous adsorption on the C-steel surface.
- Polarization curves indicated that the inhibitors are of mixed type.
- Kinetic and adsorption parameters were evaluated and are discussed.
- All tested methods confirm IE % to be in the order IL3 > IL2 > IL1
- The experimental methods are in good agreement with the theoretical calculation.

## AUTHOR INFORMATION

### Corresponding Author

Abd El-Aziz S. Fouda – Department of Chemistry, Faculty of Science, Mansoura University, Mansoura 35516, Egypt; [orcid.org/0000-0002-3239-4417](https://orcid.org/0000-0002-3239-4417); Phone: +2 050 2365730; Email: [asfouda@hotmail.com](mailto:asfouda@hotmail.com); Fax: +2 050 2202264

### Authors

Hend Asfour – Department of Chemistry, Faculty of Science, Mansoura University, Mansoura 35516, Egypt  
 Ghada Y. Elewady – Department of Chemistry, Faculty of Science, Mansoura University, Mansoura 35516, Egypt  
 Elsayed G. Zaki – Egyptian Petroleum Research Institute, Nasr City 11727 Cairo, Egypt

Complete contact information is available at: <https://pubs.acs.org/10.1021/acsomega.3c03463>

### Notes

The authors declare no competing financial interest.

## ACKNOWLEDGMENTS

The authors thank the Chemistry Department, Faculty of Science, Mansoura and Tanta Universities for the help provided.

## REFERENCES

- Abdallah, Y. M.; Hassan, H. M.; Shalabi, K.; Fouda, A. S. Effects of *Arctostaphylos Uva-Ursi* Extract as Green Corrosion Inhibitor for Cu10Ni Alloy in 1 M HNO<sub>3</sub>. *Int. J. Electrochem. Sci.* **2014**, *9*, 5073–5091.
- Abd El-Lateef, H. M.; Sayed, A. R.; Gomha, S. M.; Bakir, E. M.; Shalabi, K. Synthesis and Study of Poly [(Hydrazinylazo)] Thiazoles

- as Potent Corrosion Inhibitors for Cast Iron-Carbon Alloy in Molar HCl: A Collective Computational and Experiential Methods. *J. Mol. Liq.* **2021**, *337*, 116555.
- (3) Abd El-Lateef, H. M.; Shalabi, K.; Tantawy, A. H. Corrosion Inhibition of Carbon Steel in Hydrochloric Acid Solution Using Newly Synthesized Urea-Based Cationic Fluorosurfactants: Experimental and Computational Investigations. *New J. Chem.* **2020**, *44* (41), 17791–17814.
- (4) El-Askalany, A. H.; Mostafa, S. I.; Shalabi, K.; Eid, A. M.; Shaaban, S. Novel Tetrazole-Based Symmetrical Diselenides as Corrosion Inhibitors for N80 Carbon Steel in 1 M HCl Solutions: Experimental and Theoretical Studies. *J. Mol. Liq.* **2016**, *223*, 497–508.
- (5) Fouda, A. S.; El-Ghaffar, M. A. A.; Sherif, M. H.; El-Habab, A. T.; El-Hossiany, A. Novel Anionic 4-Tert-Octyl Phenol Ethoxylate Phosphate Surfactant as Corrosion Inhibitor for C-Steel in Acidic Media. *Prot. Met. Phys. Chem. Surf.* **2020**, *56* (1), 189–201.
- (6) Elgyar, O. A.; Ouf, A. M.; El-Hossiany, A.; Fouda, A. E. A. S. The Inhibition Action of *Viscum Album* Extract on the Corrosion of Carbon Steel in Hydrochloric Acid Solution. *Biointerface Res. Appl. Chem.* **2021**, *11* (6), 14344–14358.
- (7) Shalabi, K.; Helmy, A. M.; El-Askalany, A. H.; Shahba, M. M. New Pyridinium Bromide Mono-Cationic Surfactant as Corrosion Inhibitor for Carbon Steel during Chemical Cleaning: Experimental and Theoretical Studies. *J. Mol. Liq.* **2019**, *293*, 111480.
- (8) Fouda, A. S.; Ibrahim, H.; Rashwaan, S.; El-Hossiany, A.; Ahmed, R. M. Expired Drug (Pantoprazole Sodium) as a Corrosion Inhibitor for High Carbon Steel in Hydrochloric Acid Solution. *Int. J. Electrochem. Sci.* **2018**, *13* (7), 6327–6346.
- (9) Fouda, A. S.; El-Mekabaty, A.; Shaaban, I. E. I.; El-Hossiany, A. Synthesis and Biological Evaluation of Novel Thiophene Derivatives as Green Inhibitors for Aluminum Corrosion in Acidic Media. *Prot. Met. Phys. Chem. Surf.* **2021**, *57* (5), 1060–1075.
- (10) Zaky, M. T.; Nessim, M. I.; Deyab, M. A. Synthesis of New Ionic Liquids Based on Dicationic Imidazolium and Their Anti-Corrosion Performances. *J. Mol. Liq.* **2019**, *290*, 111230.
- (11) Ramkumar, S.; Nalini, D.; Quraishi, M. A.; Ebenso, E. E.; Verma, C. Anti-corrosive Property of Bioinspired Environmental Benign Imidazole and Isoxazoline Heterocyclics: A Cumulative Studies of Experimental and DFT Methods. *J. Heterocycl. Chem.* **2020**, *57* (1), 103–119.
- (12) Deyab, M. A. 1-Allyl-3-Methylimidazolium Bis (Trifluoromethylsulfonyle) Imide as an Effective Organic Additive in Aluminum-Air Battery. *Electrochim. Acta* **2017**, *244*, 178–183.
- (13) Zhou, T.; Yuan, J.; Zhang, Z.; Xin, X.; Xu, G. The Comparison of Imidazolium Gemini Surfactant [C14–4-C14im] Br<sub>2</sub> and Its Corresponding Monomer as Corrosion Inhibitors for A3 Carbon Steel in Hydrochloric Acid Solutions: Experimental and Quantum Chemical Studies. *Colloids Surf., A* **2019**, *575*, 57–65.
- (14) Qiang, Y.; Zhang, S.; Guo, L.; Zheng, X.; Xiang, B.; Chen, S. Experimental and Theoretical Studies of Four Allyl Imidazolium-Based Ionic Liquids as Green Inhibitors for Copper Corrosion in Sulfuric Acid. *Corros. Sci.* **2017**, *119*, 68–78.
- (15) El-Katori, E. E.; Nessim, M. I.; Deyab, M. A.; Shalabi, K. Electrochemical, XPS and Theoretical Examination on the Corrosion Inhibition Efficacy of Stainless Steel via Novel Imidazolium Ionic Liquids in Acidic Solution. *J. Mol. Liq.* **2021**, *337*, 116467.
- (16) Deyab, M. A.; Dief, H. A. A.; Eissa, E. A.; Taman, A. R. Electrochemical Investigations of Naphthenic Acid Corrosion for Carbon Steel and the Inhibitive Effect by Some Ethoxylated Fatty Acids. *Electrochim. Acta* **2007**, *52* (28), 8105–8110.
- (17) Hejazifar, M.; Lanaridi, O.; Bica-Schröder, K. Ionic Liquid Based Microemulsions: A Review. *J. Mol. Liq.* **2020**, *303*, 112264.
- (18) Yang, G.; Song, Y.; Wang, Q.; Zhang, L.; Deng, L. Review of Ionic Liquids Containing Polymer/Inorganic Hybrid Electrolytes for Lithium Metal Batteries. *Mater. Des.* **2020**, *190*, 108563.
- (19) Nasibi, M.; Zaarei, D.; Rashed, G.; Ghasemi, E. Chamomile (*Matricaria Recutita*) Extract as a Corrosion Inhibitor for Mild Steel in Hydrochloric Acid Solution. *Chem. Eng. Commun.* **2013**, *200* (3), 367–378.
- (20) Abd El-Lateef, H. M.; Shalabi, K.; Abdelhamid, A. A. One-Pot Synthesis of Novel Triphenyl Hexyl Imidazole Derivatives Catalyzed by Ionic Liquid for Acid Corrosion Inhibition of C1018 Steel: Experimental and Computational Perspectives. *J. Mol. Liq.* **2021**, *334*, 116081.
- (21) Zuriaga-Monroy, C.; Oviedo-Roa, R.; Montiel-Sánchez, L. E.; Vega-Paz, A.; Marin-Cruz, J.; Martinez-Magadan, J.-M. Theoretical Study of the Aliphatic-Chain Length's Electronic Effect on the Corrosion Inhibition Activity of Methylimidazole-Based Ionic Liquids. *Ind. Eng. Chem. Res.* **2016**, *55* (12), 3506–3516.
- (22) Jafari, H.; Mohsenifar, F.; Sayin, K. Effect of Alkyl Chain Length on Adsorption Behavior and Corrosion Inhibition of Imidazoline Inhibitors. *Iran. J. Chem. Chem. Eng.* **2018**, *37* (5), 85–103.
- (23) Subramanian, C. Localized Pitting Corrosion of API 5L Grade A Pipe Used in Industrial Fire Water Piping Applications. *Eng. Failure Anal.* **2018**, *92*, 405–417.
- (24) El Kacimi, Y.; Touir, R.; Galai, M.; Belakhmima, R. A.; Zarrouk, A.; Alaoui, K.; Harcharras, M.; El Kafssaoui, H.; Ebn Touhami, M. Effect of Silicon and Phosphorus Contents in Steel on Its Corrosion Inhibition in 5 M HCl Solution in the Presence of Cetyltrimethylammonium/KL. *J. Mater. Environ. Sci.* **2016**, *7* (1), 371–381.
- (25) Rbaa, M.; Galai, M.; Abousalem, A. S.; Lakhri, B.; Touhami, M. E.; Warad, I.; Zarrouk, A. Synthetic, Spectroscopic Characterization, Empirical and Theoretical Investigations on the Corrosion Inhibition Characteristics of Mild Steel in Molar Hydrochloric Acid by Three Novel 8-Hydroxyquinoline Derivatives. *Ionics* **2020**, *26*, 503–522.
- (26) Sasikumar, Y.; Adekunle, A. S.; Olasunkanmi, L. O.; Bahadur, I.; Baskar, R.; Kabanda, M. M.; Obot, I. B.; Ebenso, E. E. Experimental, Quantum Chemical and Monte Carlo Simulation Studies on the Corrosion Inhibition of Some Alkyl Imidazolium Ionic Liquids Containing Tetrafluoroborate Anion on Mild Steel in Acidic Medium. *J. Mol. Liq.* **2015**, *211*, 105–118.
- (27) Tawfik, S. M. Ionic Liquids Based Gemini Cationic Surfactants as Corrosion Inhibitors for Carbon Steel in Hydrochloric Acid Solution. *J. Mol. Liq.* **2016**, *216*, 624–635.
- (28) Gonzalez-Rodriguez, J. G.; Zeferino-Rodriguez, T.; Ortega, D. M.; Serna, S.; Campillo, B.; Casales, M.; Valenzuela, E.; Juárez-Islas, J. Effect of Microstructure on the CO<sub>2</sub> Corrosion Inhibition by Carboxyamidoimidazolines on a Pipeline Steel. *Int. J. Electrochem. Sci.* **2007**, *2* (11), 883–896.
- (29) El-Awady, A. A.; Abd-El-Nabey, B. A.; Aziz, S. G. Kinetic-thermodynamic and Adsorption Isotherms Analyses for the Inhibition of the Acid Corrosion of Steel by Cyclic and Open-chain Amines. *J. Electrochem. Soc.* **1992**, *139* (8), 2149–2154.
- (30) Khan, S.; Quraishi, M. A. Synergistic Effect of Potassium Iodide on Inhibitive Performance of Thiadiazoles during Corrosion of Mild Steel in 20% Sulfuric Acid. *Arab. J. Sci. Eng.* **2010**, *35* (1), 71–81.
- (31) Abd El-Lateef, H. M.; Shalabi, K.; Arab, A. M.; Abdallah, Y. M. Corrosion Mitigation Performance of N80 Steel in 5% Sulfamic Acid Medium by Applying Novel Tetrahydro-1, 2, 4-Triazines Including Triazine Moieties: Electrochemical and Theoretical Approaches. *ACS Omega* **2022**, *7* (27), 23380–23392.
- (32) Deyab, M. A. Corrosion Inhibition of Heat Exchanger Tubing Material (Titanium) in MSF Desalination Plants in Acid Cleaning Solution Using Aromatic Nitro Compounds. *Desalination* **2018**, *439*, 73–79.
- (33) Nahlé, A.; Salim, R.; El Hajjaji, F.; Ech-chihbi, E.; Titi, A.; Messali, M.; Kaya, S.; El Ibrahim, B.; Taleb, M. Experimental and Theoretical Approach for Novel Imidazolium Ionic Liquids as Smart Corrosion Inhibitors for Mild Steel in 1.0 M Hydrochloric Acid. *Arabian J. Chem.* **2022**, *15* (8), 103967.
- (34) Dehghani, A.; Mostafatabar, A. H.; Bahlakeh, G.; Ramezanzadeh, B. A Detailed Study on the Synergistic Corrosion Inhibition Impact of the Quercetin Molecules and Trivalent Europium Salt on Mild Steel; Electrochemical/Surface Studies,

DFT Modeling, and MC/MD Computer Simulation. *J. Mol. Liq.* **2020**, *316*, 113914.

(35) Eid, A. M.; Shaaban, S.; Shalabi, K. Tetrazole-Based Organoselenium Bi-Functionalized Corrosion Inhibitors during Oil Well Acidizing: Experimental, Computational Studies, and SRB Bioassay. *J. Mol. Liq.* **2020**, *298*, 111980.

(36) Kaya, S.; Guo, L.; Kaya, C.; Tüzün, B.; Obot, I. B.; Touir, R.; Islam, N. Quantum Chemical and Molecular Dynamic Simulation Studies for the Prediction of Inhibition Efficiencies of Some Piperidine Derivatives on the Corrosion of Iron. *J. Taiwan Inst. Chem. Eng.* **2016**, *65*, 522–529.

(37) Moriana, R.; Vilaplana, F.; Ek, M. Cellulose Nanocrystals from Forest Residues as Reinforcing Agents for Composites: A Study from Macro- to Nano-Dimensions. *Carbohydr. Polym.* **2016**, *139*, 139–149.

(38) Gao, G.; Liang, C. Electrochemical and DFT Studies of  $\beta$ -Amino-Alcohols as Corrosion Inhibitors for Brass. *Electrochim. Acta* **2007**, *52* (13), 4554–4559.

(39) Toghan, A.; Gouda, M.; Shalabi, K.; El-Lateef, H. M. A. Preparation, Characterization, and Evaluation of Macrocrystalline and Nanocrystalline Cellulose as Potential Corrosion Inhibitors for Ss316 Alloy during Acid Pickling Process: Experimental and Computational Methods. *Polymers* **2021**, *13* (14), 2275.

(40) Dahmani, K.; Galai, M.; Ouakki, M.; Cherkaoui, M.; Touir, R.; Erkan, S.; Kaya, S.; El Ibrahim, B. Quantum chemical and molecular dynamic simulation studies for the identification of the extracted cinnamon essential oil constituent responsible for copper corrosion inhibition in acidified 3.0 wt% NaCl medium. *Inorg. Chem. Commun.* **2021**, *124*, 108409.

(41) Wen, Y.-N.; Zhang, J.-M. Surface Energy Calculation of the Fcc Metals by Using the MAEAM. *Solid State Commun.* **2007**, *144* (3–4), 163–167.

(42) El shafiee, C.; El-Nagar, R.; Nessim, M.; Khalil, M.; Shaban, M.; Alharthy, R. D.; Ismail, D.; Abdallah, R.; Moustafa, Y. Application of Asymmetric Dicationic Ionic Liquids for Oil Spill Remediation in Sea Water. *Arabian J. Chem.* **2021**, *14* (5), 103123.

(43) Ramasamy, R. Vibrational Spectroscopic Studies of Imidazole. *Arm. J. Phys.* **2015**, *8*(1) 51–55.

(44) Zhao, T.; Mu, G. The Adsorption and Corrosion Inhibition of Anion Surfactants on Aluminium Surface in Hydrochloric Acid. *Corros. Sci.* **1999**, *41* (10), 1937–1944.

(45) Mobin, M.; Rizvi, M. Polysaccharide from Plantago as a Green Corrosion Inhibitor for Carbon Steel in 1 M HCl Solution. *Carbohydr. Polym.* **2017**, *160*, 172–183.

(46) Othman, N. A.; Ali, A. M. M.; Samsi, N. S.; Salim, F.; Panuh, D.; Yaakob, M. K.; Embong, Z.; Md Sauri, A. S.; Che Isa, N. N.; Nor Hashim, N. Z. Environmentally Conscience Corrosion Inhibitors for Mild Steel in Corrosive Hydrochloric Acid Solution by Uncaria Cordata Extract: Experimental and Theoretical Studies. *J. Adhes. Sci. Technol.* **2023**, 1–29.

(47) James, A. O.; Oforka, N. C.; Abiola, O. K. Inhibition of Acid Corrosion of Mild Steel by Pyridoxal and Pyridoxol Hydrochlorides. *Int. J. Electrochem. Sci.* **2007**, *2*, 278–284.

(48) Obi-Egbedi, N. O.; Obot, I. B. Inhibitive Properties, Thermodynamic and Quantum Chemical Studies of Alloxazine on Mild Steel Corrosion in H<sub>2</sub>SO<sub>4</sub>. *Corros. Sci.* **2011**, *53* (1), 263–275.

(49) Abd El-Rehim, S. S.; Hassan, H. H.; Deyab, M. A. M.; Abd El Moneim, A. Experimental and Theoretical Investigations of Adsorption and Inhibitive Properties of Tween 80 on Corrosion of Aluminum Alloy (A5754) in Alkaline Media. *Z. Phys. Chem.* **2016**, *230* (1), 67–78.

(50) Döner, A.; Kardaş, G. N-Aminorhodanine as an Effective Corrosion Inhibitor for Mild Steel in 0.5 M H<sub>2</sub>SO<sub>4</sub>. *Corros. Sci.* **2011**, *53* (12), 4223–4232.

(51) Fouda, A. S.; Ismail, M. A.; Khaled, M. A.; El-Hossiany, A. A. Experimental and Computational Chemical Studies on the Corrosion Inhibition of New Pyrimidinone Derivatives for Copper in Nitric Acid. *Sci. Rep.* **2022**, *12* (1), 16089.

(52) Zaidon, F. H.; Kassim, K.; Mohd Zaki, H.; Embong, Z.; Anouar, E. H.; Nor Hashim, N. Z. Adsorption and Corrosion

Inhibition Accomplishment for Thiosemicarbazone Derivatives for Mild Steel in 1.0 M HCl Medium: Electrochemical, XPS and DFT Studies. *J. Mol. Liq.* **2021**, *329*, 115553.

(53) Ansari, K. R.; Quraishi, M. A.; Singh, A. Schiff's Base of Pyridyl Substituted Triazoles as New and Effective Corrosion Inhibitors for Mild Steel in Hydrochloric Acid Solution. *Corros. Sci.* **2014**, *79*, 5–15.

(54) Wang, Y.; Wang, J.; Ma, L.; Ren, C.; Zhang, D.; Ma, L.; Sun, M. Qualitative and Quantitative Detection of Corrosion Inhibitors Using Surface-Enhanced Raman Scattering Coupled with Multivariate Analysis. *Appl. Surf. Sci.* **2021**, *568*, 150967.

(55) Li, X.; Deng, S.; Fu, H. Inhibition by Tetradecylpyridinium Bromide of the Corrosion of Aluminium in Hydrochloric Acid Solution. *Corros. Sci.* **2011**, *53* (4), 1529–1536.

(56) Fawcett, W. R.; Kováčová, Z.; Motheo, A. J.; Foss, C. A. Application of the Ac Admittance Technique to Double-Layer Studies on Polycrystalline Gold Electrodes. *J. Electroanal. Chem.* **1992**, *326* (1–2), 91–103.

(57) Veloz, M. A.; Gonzalez, I. Electrochemical Study of Carbon Steel Corrosion in Buffered Acetic Acid Solutions with Chlorides and H<sub>2</sub>S. *Electrochim. Acta* **2002**, *48* (2), 135–144.

(58) Qian, B.; Wang, J.; Zheng, M.; Hou, B. Synergistic Effect of Polyspartic Acid and Iodide Ion on Corrosion Inhibition of Mild Steel in H<sub>2</sub>SO<sub>4</sub>. *Corros. Sci.* **2013**, *75*, 184–192.

(59) Haruna, K.; Saleh, T. A.; Quraishi, M. A. Expired Metformin Drug as Green Corrosion Inhibitor for Simulated Oil/Gas Well Acidizing Environment. *J. Mol. Liq.* **2020**, *315*, 113716.

(60) Oguzie, E. E.; Li, Y.; Wang, F. H. Effect of 2-Amino-3-Mercaptopropanoic Acid (Cysteine) on the Corrosion Behaviour of Low Carbon Steel in Sulphuric Acid. *Electrochim. Acta* **2007**, *53* (2), 909–914.

(61) Deyab, M. A.; Ouarsal, R.; Al-Sabagh, A. M.; Lachkar, M.; El Bali, B. Enhancement of Corrosion Protection Performance of Epoxy Coating by Introducing New Hydrogenphosphate Compound. *Prog. Org. Coatings* **2017**, *107*, 37–42.

(62) Ali, M. A.; Ouf, A. M.; El-Hossiany, A.; Fouda, A. Eco-Friendly Approach to Corrosion Inhibition of Copper in HNO<sub>3</sub> Solution by the Expired Tylosin Drug. *Biointerface Res. Appl. Chem.* **2022**, *12* (4), 5116–5130.

(63) Habibiyan, A.; Ramezanzadeh, B.; Mahdavian, M.; Kasaeian, M. Facile Size and Chemistry-Controlled Synthesis of Mussel-Inspired Bio-Polymers Based on Polydopamine Nanospheres: Application as Eco-Friendly Corrosion Inhibitors for Mild Steel against Aqueous Acidic Solution. *J. Mol. Liq.* **2020**, *298*, 111974.

(64) Mobin, M.; Zehra, S.; Parveen, M. L-Cysteine as Corrosion Inhibitor for Mild Steel in 1 M HCl and Synergistic Effect of Anionic, Cationic and Non-Ionic Surfactants. *J. Mol. Liq.* **2016**, *216*, 598–607.

(65) El Hamdani, N.; Fdil, R.; Tourabi, M.; Jama, C.; Bentiss, F. Alkaloids Extract of Retama Monosperma (L.) Boiss. Seeds Used as Novel Eco-Friendly Inhibitor for Carbon Steel Corrosion in 1 M HCl Solution: Electrochemical and Surface Studies. *Appl. Surf. Sci.* **2015**, *357*, 1294–1305.

(66) Wang, X.; Yang, W.; Li, F.; Xue, Y.; Liu, R.; Hao, Y. In Situ Microwave-Assisted Synthesis of Porous N-TiO<sub>2</sub>/g-C<sub>3</sub>N<sub>4</sub> Heterojunctions with Enhanced Visible-Light Photocatalytic Properties. *Ind. Eng. Chem. Res.* **2013**, *52* (48), 17140–17150.

(67) Fouda, A. e.; El-Aal, A.; Sliem, M.; Abdullah, A. Caprylamidopropyl Betaine as a Highly Efficient Eco-Friendly Corrosion Inhibitor for API X120 Steel in 1 M H<sub>2</sub>SO<sub>4</sub>. *Egypt. J. Chem.* **2020**, *63* (3), 759–776.

(68) Lagrenee, M.; Mernari, B.; Bouanis, M.; Traisnel, M.; Bentiss, F. Study of the Mechanism and Inhibiting Efficiency of 3, 5-Bis (4-Methylthiophenyl)-4H-1, 2, 4-Triazole on Mild Steel Corrosion in Acidic Media. *Corros. Sci.* **2002**, *44* (3), 573–588.

(69) Arellanes-Lozada, P.; Olivares-Xometl, O.; Likhanova, N. V.; Lijanova, I. V.; Vargas-García, J. R.; Hernández-Ramírez, R. E. Adsorption and Performance of Ammonium-Based Ionic Liquids as Corrosion Inhibitors of Steel. *J. Mol. Liq.* **2018**, *265*, 151–163.

(70) Singh, A.; Ansari, K. R.; Chauhan, D. S.; Quraishi, M. A.; Lgaz, H.; Chung, I.-M. Comprehensive Investigation of Steel Corrosion

Inhibition at Macro/Micro Level by Ecofriendly Green Corrosion Inhibitor in 15% HCl Medium. *J. Colloid Interface Sci.* **2020**, *560*, 225–236.

(71) Boulhaoua, M.; El Hafi, M.; Zehra, S.; Eddaif, L.; Alrashdi, A. A.; Lahmidi, S.; Guo, L.; Mague, J. T.; Lgaz, H. Synthesis, Structural Analysis and Corrosion Inhibition Application of a New Indazole Derivative on Mild Steel Surface in Acidic Media Complemented with DFT and MD Studies. *Colloids Surf., A* **2021**, *617*, 126373.

(72) El-Taib Heikal, F.; Deyab, M. A.; Osman, M. M.; Nessim, M. I.; Elkholi, A. E. Synthesis and Assessment of New Cationic Gemini Surfactants as Inhibitors for Carbon Steel Corrosion in Oilfield Water. *RSC Adv.* **2017**, *7* (75), 47335–47352.

(73) Gece, G.; Bilgiç, S. Quantum Chemical Study of Some Cyclic Nitrogen Compounds as Corrosion Inhibitors of Steel in NaCl Media. *Corros. Sci.* **2009**, *51* (8), 1876–1878.

(74) Palaniappan, N.; Cole, I. S.; Kuznetsov, A. E. Experimental and Computational Studies of Graphene Oxide Covalently Functionalized by Octylamine: Electrochemical Stability, Hydrogen Evolution, and Corrosion Inhibition of the AZ13 Mg Alloy in 3.5% NaCl. *Rsc Adv.* **2020**, *10* (19), 11426–11434.

(75) Obot, I. B.; Macdonald, D. D.; Gasem, Z. M. Density Functional Theory (DFT) as a Powerful Tool for Designing New Organic Corrosion Inhibitors. Part 1: An Overview. *Corros. Sci.* **2015**, *99*, 1–30.

(76) Lukovits, I.; Kalman, E.; Zucchi, F. Corrosion Inhibitors—Correlation between Electronic Structure and Efficiency. *Corrosion* **2001**, *57* (1), 3–8.

(77) Upadhyay, A.; Purohit, A. K.; Mahakur, G.; Dash, S.; Kar, P. K. Verification of Corrosion Inhibition of Mild Steel by Some 4-Aminoantipyrine-Based Schiff Bases-Impact of Adsorbate Substituent and Cross-Conjugation. *J. Mol. Liq.* **2021**, *333*, 115960.

(78) Obot, I. B.; Kaya, S.; Kaya, C.; Tüzün, B. Density Functional Theory (DFT) Modeling and Monte Carlo Simulation Assessment of Inhibition Performance of Some Carbohydrazide Schiff Bases for Steel Corrosion. *Phys. E* **2016**, *80*, 82–90.

(79) Jmiai, A.; Tara, A.; El Issami, S.; Hilali, M.; Jbara, O.; Bazzi, L. A New Trend in Corrosion Protection of Copper in Acidic Medium by Using Jujube Shell Extract as an Effective Green and Environmentally Safe Corrosion Inhibitor: Experimental, Quantum Chemistry Approach and Monte Carlo Simulation Study. *J. Mol. Liq.* **2021**, *322*, 114509.

(80) Madkour, L. H.; Kaya, S.; Obot, I. B. Computational, Monte Carlo Simulation and Experimental Studies of Some Arylazotriazoles (AATR) and Their Copper Complexes in Corrosion Inhibition Process. *J. Mol. Liq.* **2018**, *260*, 351–374.

(81) Mary, Y. S.; Panicker, C. Y.; Sapnakumari, M.; Narayana, B.; Sarojini, B. K.; Al-Saadi, A. A.; Van Alsenoy, C.; War, J. A. FT-IR, NBO, HOMO-LUMO, MEP Analysis and Molecular Docking Study of 1-[3-(4-Fluorophenyl)-5-Phenyl-4, 5-Dihydro-1H-Pyrazol-1-Yl] Ethanone. *Spectrochim. Acta, Part A* **2015**, *136*, 483–493.

(82) Kumar, H.; Dhanda, T. Cyclohexylamine an Effective Corrosion Inhibitor for Mild Steel in 0.1 N H<sub>2</sub>SO<sub>4</sub>: Experimental and Theoretical (Molecular Dynamics Simulation and FMO) Study. *J. Mol. Liq.* **2021**, *327*, 114847.

(83) Bouoidina, A.; Ech-Chihbi, E.; El-Hajjaji, F.; El Ibrahim, B.; Kaya, S.; Taleb, M. Anisole Derivatives as Sustainable-Green Inhibitors for Mild Steel Corrosion in 1 M HCl: DFT and Molecular Dynamic Simulations Approach. *J. Mol. Liq.* **2021**, *324*, 115088.

(84) Ramalingam, S.; David Suresh Babu, P.; Periandy, S.; Fereyduni, E. Vibrational Investigation, Molecular Orbital Studies and Molecular Electrostatic Potential Map Analysis on 3-Chlorobenzoic Acid Using Hybrid Computational Calculations. *Spectrochim. Acta, Part A* **2011**, *84* (1), 210–220.

(85) Aadad, H. E.; Galai, M.; Ouakki, M.; Elgendy, A.; Touhami, M. E.; Chahine, A. Improvement of the Corrosion Resistance of Mild Steel in Sulfuric Acid by New Organic-Inorganic Hybrids of Benzimidazole-Pyrophosphate: Facile Synthesis, Characterization, Experimental and Theoretical Calculations (DFT and MC). *Surf. Interfaces* **2021**, *24*, 101084.

(86) Bereket, G.; Pinarbaşı, A. Electrochemical Thermodynamic and Kinetic Studies of the Behaviour of Aluminium in Hydrochloric Acid Containing Various Benzotriazole Derivatives. *Corros. Eng., Sci. Technol.* **2004**, *39* (4), 308–312.

(87) Hulsbosch, J.; De Vos, D. E.; Binnemans, K.; Ameloot, R. Biobased Ionic Liquids: Solvents for a Green Processing Industry? *ACS Sustain. Chem. Eng.* **2016**, *4* (6), 2917–2931.

(88) Behpour, M.; Ghoreishi, S. M.; Salavati-Niasari, M.; Ebrahimi, B. Evaluating Two New Synthesized S-N Schiff Bases on the Corrosion of Copper in 15% Hydrochloric Acid. *Mater. Chem. Phys.* **2008**, *107* (1), 153–157.

(89) El Mehdi, B.; Mernari, B.; Traisnel, M.; Bentiss, F.; Lagreene, M. Synthesis and Comparative Study of the Inhibitive Effect of Some New Triazole Derivatives towards Corrosion of Mild Steel in Hydrochloric Acid Solution. *Mater. Chem. Phys.* **2003**, *77* (2), 489–496.

(90) Yurt, A.; Balaban, A.; Kandemir, S. U.; Bereket, G.; Erk, B. Investigation on Some Schiff Bases as HCl Corrosion Inhibitors for Carbon Steel. *Mater. Chem. Phys.* **2004**, *85* (2–3), 420–426.

(91) Singh, A. K.; Quraishi, M. A. Adsorption Properties and Inhibition of Mild Steel Corrosion in Hydrochloric Acid Solution by Ceftobiprole. *J. Appl. Electrochem.* **2011**, *41* (1), 7–18.